

A Multihop Graph Rectify Attention and Spectral Overlap Grouping Convolutional Fusion Network for Hyperspectral Image Classification

Cuiping Shi¹, Member, IEEE, Shuheng Yue², Haiyang Wu², Fei Zhu², and Ligu Wang³, Member, IEEE

Abstract—Convolutional neural networks (CNNs) have been widely used in hyperspectral image (HSI) classification due to their ability to extract image features effectively. However, under the condition of limited samples, the modeling ability of CNNs for the relationships among samples is limited. At present, research on the classification of HSIs with a small number of samples remains an important challenge in the field of HSI processing. Recently, graph convolutional networks (GCNs) have been applied in HSI classification tasks. In this article, a multihop graph rectifies attention and spectral overlap grouping convolutional fusion network (MRSGFN) for HSI classification is proposed. In the graph convolution branch, a multihop graph rectify attention (MHRA) is designed to weight and correct the features extracted by graph convolution. In the convolutional branch, to solve the problem of dimensionality disaster caused by high spectral dimension with a small number of samples, a spectral intra group inter group feature extraction module (SI2FEM) based on spectral overlap grouping is constructed. In order to better fuse the features extracted from CNNs and GCNs, a Gaussian weighted fusion module (GWFM) is elaborately designed in this article. The features extracted by different branches are assigned different weights by GWFM through a 2-D Gaussian map and then fused. Numerous experiments were conducted on three common datasets and showed that the classification performance of the proposed MRSGFN is superior to other advanced methods.

Index Terms—Convolutional neural networks (CNNs), few samples, graph convolution, hyperspectral image (HSI) classification.

I. INTRODUCTION

IN THE past few decades, hyperspectral-imaging technology has experienced rapid development and has been widely applied in various fields such as biomedical [1], [2], precision agriculture [3], and vegetation exploration [1], [4].

Manuscript received 8 March 2024; revised 19 May 2024; accepted 5 June 2024. Date of publication 11 June 2024; date of current version 20 June 2024. This work was supported in part by the National Natural Science Foundation of China under Grant 42271409 and Grant 62071084. (Corresponding author: Cuiping Shi.)

Cuiping Shi is with the Department of Communication Engineering, Qiqihar University, Qiqihar 161000, China, and also with the College of Information Engineering, Huzhou University, Huzhou 313000, China (e-mail: shicuiiping@qqhru.edu.cn).

Shuheng Yue, Haiyang Wu, and Fei Zhu are with the Department of Communication Engineering, Qiqihar University, Qiqihar 161000, China (e-mail: 2021910320@qqhru.edu.cn; 2021910323@qqhru.edu.cn; 2022935750@qqhru.edu.cn).

Ligu Wang is with the College of Information and Communication Engineering, Dalian Nationalities University, Dalian 116000, China (e-mail: wangliguo@hrbeu.edu.cn).

Digital Object Identifier 10.1109/TGRS.2024.3412131

The use of hyperspectral images (HSIs) for land cover classification is a challenging topic in Earth science and remote sensing. HSIs are characterized by high spectral resolution and rich spatial information. By capturing the differences in spectral features related to pixels, they can more effectively classify land features.

With the development of deep learning technology, numerous advanced deep learning networks have been applied in the field of HSIs classification and have made significant progress [5], [6], [7], [8], [9], [10], [11], [12], [13], [14], [15]. Convolutional neural networks (CNNs) are highly favored by researchers in the field of remote sensing due to their advantages of weight sharing and translation invariance [16], [17], [18], [19], [20], [21]. Roy et al. [22] proposed an attention-based adaptive spectral space kernel residual network A2S2K ResNet for HSI classification. In A2S2K ResNet, an attention-based adaptive spectral space kernel module was designed, which can adaptively select 3-D convolution kernels. Wei et al. [23] designed quaternion CNNs (QCNNs). QCNN can extract quaternion features from data and represent the structural information of HSIs through quaternion algebra. The ability of CNNs to extract image features is limited by the size of the convolutional receptive field. Based on this issue, Shi et al. [24] proposed a CNN feedback expansion convolution network (FECNet) based on dilated convolution. An extended convolution block was designed to expand the receptive field by utilizing the feature of dilated convolution. FECNet can expand the receptive field without increasing computational complexity. In order to solve the problem of end-to-end feature learning and transfer learning with limited labeled samples for HSI classification, Wang et al. [45] proposed a unified multiscale learning framework (UML) based on fully convolutional networks, which design a multiscale spatial channel attention mechanism and a multiscale shuffle block to address the problem of land-cover map distortion. Deformable convolution has the advantage of a receptive field that can better fit the target object. It can adjust the receptive field of convolution by learning the features of the target object. Zhu et al. [25] utilized the advantages of deformable convolution and proposed deformable HSI classification networks (DHCNet) based on deformable convolution. Transformers have a global receptive field and can effectively capture long-range dependencies [26], [27]. Although traditional convolution has excellent feature extraction capabilities,

it is not good at modeling long contextual information in high-resolution remote sensing images (HRRSIs). To address this issue, Tang et al. [43] proposed the W-shaped hierarchical network (WNet) by combining CNN and transformer. The idea of deformability was introduced by WNet into Siamese CNN and transformer to understand key and irregular regions in HRRSI. Ji et al. [44] integrated the respective inductive bias from CNNs and global receptive field from transformers, and proposed a spatial spectral feature extraction network with patch attention module (PAM) (PASSNet). The PAM proposed by PASSNet is integrated into CNN and transformer, and spatial spectral features are extracted from multiple perspectives. The spectral spatial feature tokenization transformer (SSFTT) was proposed by Sun et al. [28]. In SSFTT, a Gaussian weighting module is proposed that can transform shallow spatial spectral features into tokenized semantic features. Spectral feature extraction of HSIs is reconsidered from the perspective of spectral sequences. Hong et al. [29] proposed SpectralFormer (SF). SF proposed a spectral grouping-embedding module that can learn richer local spectral representations. Hong et al. [29] proposed SF. SF proposed a spectral grouping-embedding module that can learn richer local spectral representations. Although the deep learning methods based on Euclidean data for feature modeling have achieved significant results. However, feature-modeling methods based on Euclidean data are difficult to learn complex topological structures. Therefore, researchers have gradually drawn attention to feature learning methods based on graph data, such as graph CNNs [30], [31], [32], graph attention networks [13], [33], [34].

The existing HSIs classification based on unsupervised and semisupervised neural networks lacks lightweight design and incurs high computational costs. To address this issue, Zhu et al. [46] proposed a self-supervised contrastive effective asymmetric dilated network (SC-EADNet) for HSI classification. A plug and play asymmetric dilated convolution (EADC) block was designed, which uses different dilation rates to capture spatial information of objects of different shapes and sizes. To address the issues of prototype instability and domain shift between training and testing datasets in prototype based few shot learning methods, Liu et al. [47] integrated contrastive learning and few shot learning into end-to-end networks and proposed a refined prototypical contrastive learning network for few-shot learning (RPCL-FSL) for small sample HSIs classification. The existing multimodal classification methods do not fully utilize the features of multiple models. In order to solve this problem, Xu et al. [48] proposed a dual band dynamic modulation network for hyperspectral (HS) and light detection and ranging (LiDAR) data classification. A new dynamic multimodal gradient optimization (DMGO) strategy has been designed, which can adaptively control the gradient modulation of each feature extraction branch.

In recent years, graph convolutional networks (GCNs) have been widely used in HSIs classification tasks due to their powerful feature learning capabilities. GCNs can construct relationships between samples and effectively process graph structured data. First, the superpixel-based method converts image data into graph data, and then GCNs are used to extract spectral spatial features from the graph data. Shahraki

and Prasad [35] proposed a cascaded 1-DCNN and GCN method for HSI classification. Qin et al. [36] extended the original GCN to the second order, taking into account spectral and spatial neighborhood information. To solve the problem of adjacency matrix consuming a large amount of memory resources in GCN. Liu et al. [37] proposed a fast dynamic graph convolution and CNN parallel network (FDGC). A new dynamic GCN module is proposed in FDGC. It can adaptively capture topology information, and GCN is extended to large graphs. Dong et al. [12] proposed CNNs and graph attention weighted fusion networks (WFCG) by combining the advantages of CNN and GCN. The features extracted by CNN and GCN are fused through weighted fusion for final classification to better combine the features extracted by CNN and GCN. Zhou et al. [38] proposed attention multihop graph and multiscale convolutional fusion network (AMGCFN). AMGCFN proposes a multihop graph to expand the narrow receptive field of GCN, and forms a cascaded network by stacking multihop graphs GCN, which can effectively extract structural information.

Although GCN has been widely used in HSI classification, its narrow receptive field affects its feature extraction ability. Due to the hundreds of spectral bands of HSIs, dimensional disasters are easily caused in small sample situations. To address the aforementioned issues, this article proposes a multihop graph rectifies attention and spectral overlap grouping convolutional fusion network (MRSGFN) for HSI classification. First, in the GCN branch, a multihop graph rectify attention module (MHRA) is proposed. By using high-order skip plots to obtain a larger receptive field, the information from the larger receptive field is used to weight and correct the information from the smaller receptive field. Then, in the CNN branch, in order to solve the problem of dimensionality disaster caused by spectral dimensions in small samples, this article designs an spectral intra group inter group feature extraction module (SI2FEM) based on spectral overlap grouping. First, HSIs are grouped into spectral information by SI2FEM with a fixed step size and number of spectral groups. Then, in order to fully extract spectral information, SI2FEM extracts and compresses the intragroup spectral information. Finally, intergroup spectral information is extracted. In order to better fuse the features extracted by CNN and GCN, this article proposes a Gaussian weighted fusion module (GWFM). GWFM assigns different weights to the features extracted from the convolutional branch and graph convolutional branch through 2-D Gaussian mapping and then fuse the features extracted from the two branches based on the assigned weights. Finally, the fused features are sent to feedback high-order gated convolution for feature extraction.

The main contributions of this article are as follows.

- 1) In this article, a MHRA is proposed for HSI classification. Considering the characteristic of large receptive field in high-order hop graph, some attention maps are obtained by MHRA through high-order hop graph and node feature mapping. Then, attention weighting is applied to the features extracted from the first-order hop graph. The receptive field of GCN is expanded by MHRA in a high-order hop graph weighted form.

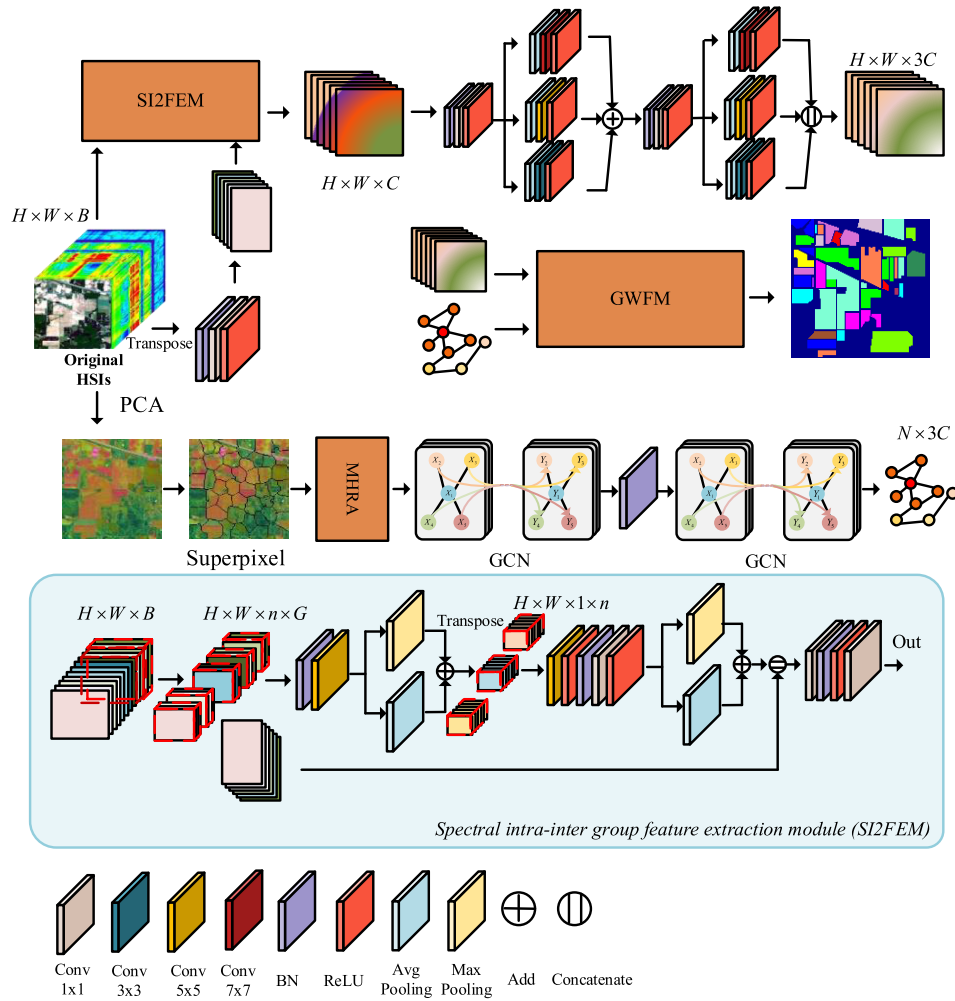


Fig. 1. Overall structure block diagram of MRS GFN.

- 2) In order to solve the problem of dimensionality disaster caused by high spectral dimension with few samples, a SI2FEM based on spectral overlap grouping is proposed. The spectra of HSIs are grouped by spectral overlap to reduce spectral dimensionality.
- 3) In order to better fuse the features extracted by CNN and GCN, a GWFM is carefully designed. Through a 2-D Gaussian mapping, GWFM assigns different weights to the features extracted by the convolution branch and graph integration branch. Then, the features extracted by different branches are fused and sent to feedback recursive gated convolution.

II. METHODOLOGY

The input HSI is represented as X in $\mathbb{R}^{H \times W \times B}$, where $H \times W$ represents the spatial size of the input data and B represents the spectral band number of HSIs. The MRS GFN method proposed in this article mainly consists of three parts, namely the SI2FEM, MHRA, and GWFM. First, a method based on superpixel segmentation is used to convert image data into graph data, which are input into the GCN branch and expanded by MHRA in the form of high-order hop graph

to enhance the receptive field of GCN. Next, the HSI data are input into the CNN branch, and SI2FEM is utilized for spectral feature extraction and dimensionality reduction. Finally, the features extracted by the two branches are input into GWFM for information weighted fusion. The overall structure diagram of MRS GFN is shown in Fig. 1.

A. SI2FEM

For HSI classification with small samples, the problem of dimensionality disaster more prominent due to the high spectral dimensions in small samples. To solve this problem, a SI2FEM is proposed in this article. The spectra of HSIs are grouped with a fixed step size and number of grouping bands through overlapping grouping. Then, in order to fully extract spectral information, a feature extraction module within and between spectral groups was designed. The structural diagram of SI2FEM is shown in Fig. 2.

First, the input HSIs data are represented as X in $\mathbb{R}^{H \times W \times B}$. HSIs data are spectral grouped, and the size of the grouped data is represented as $H \times W \times n \times c$, where n is the number of spectral groups after spectral grouping, and c is the number of spectra within a group. The calculation formula is

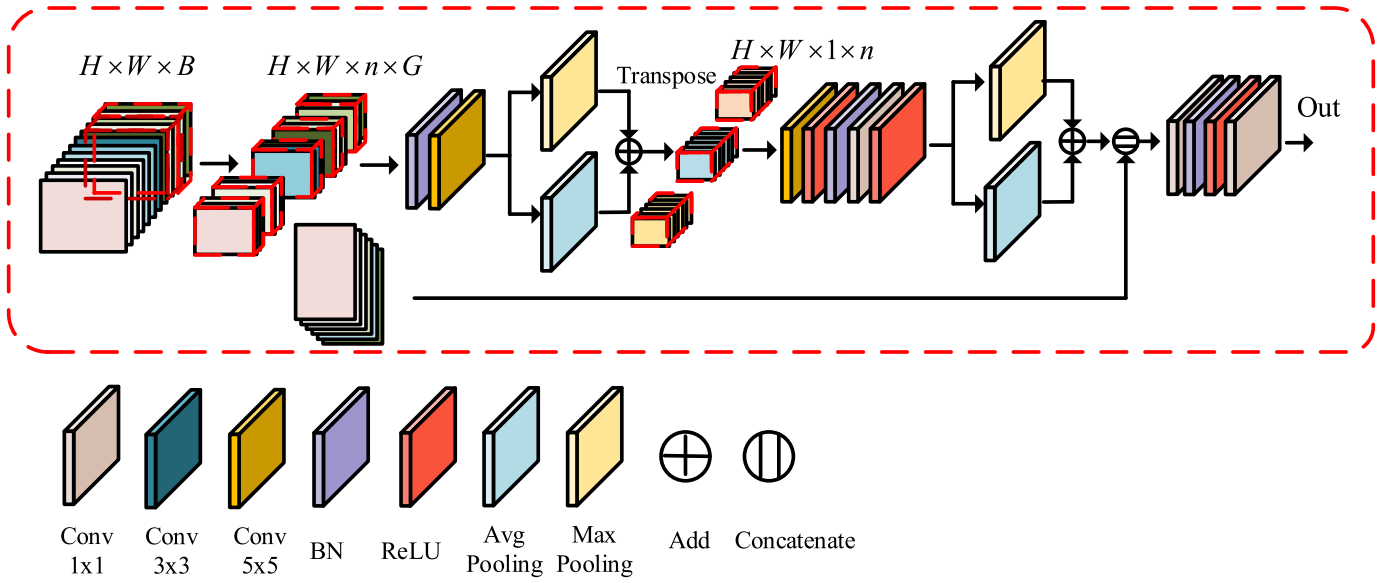


Fig. 2. Structural block diagram of SI2FEM.

as follows:

$$n = \left\lceil \frac{B}{c} \right\rceil + 1. \quad (1)$$

The specific implementation process of spectral overlap grouping is listed in Algorithm 1.

Algorithm 1 The Implementation Process of Spectral Overlap Grouping

Input: HSIs data $X \in \mathbb{R}^{H \times W \times B}$, spectral grouping number n , spectral grouping step size s

Output: HSIs data $X_g \in \mathbb{R}^{H \times W \times n \times c}$ after grouping

- 1 Calculate the spectral dimension to obtain $Bnums$
 - 2 Initialization $index = 0$
 - 3 While $index + n < Bnums$:
 - 4 The spectra from positions $index$ to $index + n$ are grouped
 - 5 Update $index = index * s$
 - 6 Determine if there are still spectra that have not been grouped. If available, repeat grouping the ungrouped spectra.
 - 7 The grouped hyperspectral data is output
- End

The data after spectral overlap grouping are input into SI2FEM for spectral extraction. The input data size of SI2FEM is represented as $H \times W \times n \times c$. First, SI2FEM performs intragroup spectral feature extraction on the input data; then, the extracted features are dimensionally reduced and transposed. The obtained feature size is $H \times W \times 1 \times n$. The process of extracting intragroup spectral information for SI2FEM can be represented as

$$X_1 = W_{1 \times 1 \times 5} \times \text{BN}(X) + b \quad (2)$$

$$X_2 = [\text{Max}(X_1) + \text{Avg}(X_1)]^{\text{Transpose}}. \quad (3)$$

Subsequently, the extracted features are subjected to intergroup spectral information extraction and dimensionality reduction. Finally, the spectral information extracted within

and between groups after grouping is corrected by cascading it with the ungrouped spectral information. The process of extracting intergroup spectral information for SI2FEM can be represented as

$$X_3 = \delta(W_{1 \times 1 \times 1} \times (\text{BN}(\delta(W_{1 \times 1 \times 5} \times X_2 + b)))) + b \quad (4)$$

$$X_4 = \text{Max}(X_3) + \text{Avg}(X_3) \quad (5)$$

$$X_{\text{out}} = W_{1 \times 1 \times 1} \times \delta(W_{1 \times 1 \times 1} \times \text{BN}(\text{Concat}(X_4, X)) + b) + b. \quad (6)$$

The batch normalization, maximum pooling function, and mean pooling function are represented as $\text{BN}(\cdot)$, $\text{Max}(\cdot)$, and $\text{Avg}(\cdot)$, respectively. $W_{1 \times 1 \times 5}$ and $W_{1 \times 1 \times 1}$ represent the convolution weights with kernel sizes of $1 \times 1 \times 5$ and $1 \times 1 \times 1$, respectively. b represents convolutional bias. $\text{Concat}(\cdot)$ represents a cascade function, and δ represents a linear rectification function.

B. Multihop Graph Rectify Attention

GCN can effectively extract local features of images by utilizing their spatial relationships and topological structures. Due to the fact that GCN is based on graph structure for feature extraction, the receptive field of each node only includes its neighboring nodes, which make the receptive field of GCN relatively narrow. In order to expand the receptive field of GCN and enable it to capture global contextual information, a MHRA is proposed in this article. MHRA obtains a larger receptive field through high-order skip maps, and then uses attention correction to weight the extracted features under the first-order skip map. The structural diagram of MHRA is shown in Fig. 3.

First, a simple linear iterative clustering (SLIC) is used for superpixel segmentation to generate superpixel map nodes. After superpixel segmentation, the resulting undirected graph structure is represented as $\mathcal{G} = (\mathcal{V}, \xi)$, where \mathcal{V} represents the vertex set of $|\mathcal{V}| = N$, and ξ represents the edge set of the

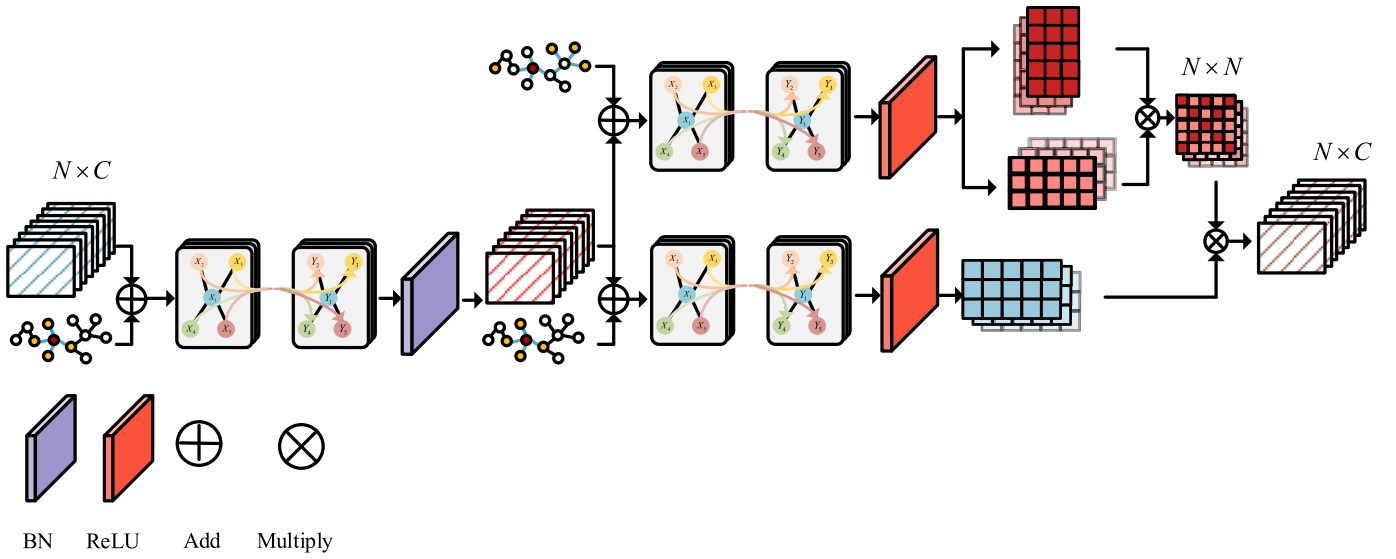


Fig. 3. Structural block diagram of MHRA.

graph. Finally, ξ and \mathcal{V} are encoded into node matrix H and adjacency matrix A , respectively, and input into GCN.

In order to obtain more receptive fields, a high-order hop graph are constructed in this article as adjacency matrices for mapping attention maps. Specifically, first, the segmentation map is obtained through SLIC. Then, the Gaussian kernel function is adopted to calculate the weights between each superpixel node, resulting in a basic weight matrix W . Finally, the adjacency matrix of the multihop graph structure is constructed using the depth first search algorithm (DFS). This process can be represented as

$$W(i, j) = \begin{cases} e^{-\|S_i - S_j\|^2} & S_j \text{ in } \mathfrak{N}(S_i) \\ 0 & \text{otherwise} \end{cases} \quad (7)$$

$$A_k(n, n_k) = \frac{1}{k}(W(n, n_1) + W(n_1, n_2) + \dots + W(n_{k-1}, n_k)) \quad (8)$$

where $\mathfrak{N}(S_i)$ is the adjacent pixel of S_j . The Euclidean distance between nodes i and j is represented as $\|S_i - S_j\|$. The middle node of the path is represented as $n, n_1, n_2, \dots, n_{k-1}, n_k$.

In the proposed MHRA module, based on the construction method of the adjacency matrix of the multihop graph structure, the first-order hop graph adjacency matrix A_1 and the fifth-order hop graph adjacency matrix A_5 were constructed and used as inputs for the adjacency matrix of MHRA. First, the node matrix H and the first-order hop graph adjacency matrix A_1 are input into GCN to extract local features. The obtained node feature matrix H_1 is also input into GCN, and after nonlinear activation, the node feature matrix H_2 is output. Then, the high-order hop graph adjacency matrices A_5 and H_1 are mapped through GCN to obtain the Query vector and Key vector. Next, the two mapped vectors are cross multiplied to obtain the attention weight matrix M_a . Finally, perform weighted rectify on the attention weight matrix M_a and the node feature matrix H_2 . The weighted corrected node feature matrix is represented as H_{out} . The calculation process is represented as

$$H_1 = \text{BN}(\text{GCN}(H, A_1)) \quad (9)$$

$$H_2 = \delta(\text{GCN}(H_1, A_1)) \quad (10)$$

$$\text{Query, Key} = \delta(\text{GCN}(H_1, A_5)) \quad (11)$$

$$H_{out} = H_1 \times (\text{Query} \otimes \text{Key}). \quad (12)$$

Among them, the graph convolution is represented as $\text{GCN}(\cdot)$. H, H_1 and H_2 represent node matrices at different stages. The first-order hop graph adjacency matrix and the fifth-order hop graph adjacency matrix are represented as A_1 and A_5 , respectively.

C. Gaussian Weighted Fusion Module

The MRSGFN proposed in this article is a dual branch fusion network. In [39], it is indicated that the discriminative regions correspond to the most sensitive features, while the secondary features represent important but easily overlooked regions. Sensitive features are beneficial for enhancing decision-making ability, while secondary features are also beneficial for better classification. In order to better combine the advantages of CNN and GCN, based on our previous work [26], this article proposes a GWFM. First, the features extracted from the two branches are weighted by GWFM for channel information. Then, the attention matrix is weighted twice by GWFM through a 2-D Gaussian function mapping, which can better suppress unimportant features and enhance important and subimportant features. Next, the weighted fused features are sent to the feedback recursive gated convolution module for feature extraction again. Finally, the output features are sent to the classifier for classification. The structural diagram of GWFM is shown in Fig. 4.

In order to better fuse the features extracted by graph convolution with those extracted by convolution, inspired by Liu et al. [40], a mutual conversion between graph data and superpixel data is conducted in the network. In the preprocessing stage of HSI, the image data are processed using superpixel segmentation method, and a transformation matrix Q in $\mathbb{R}^{H \times Z}$ between pixels and superpixels is constructed, where Z represents the number of superpixels. The calculation

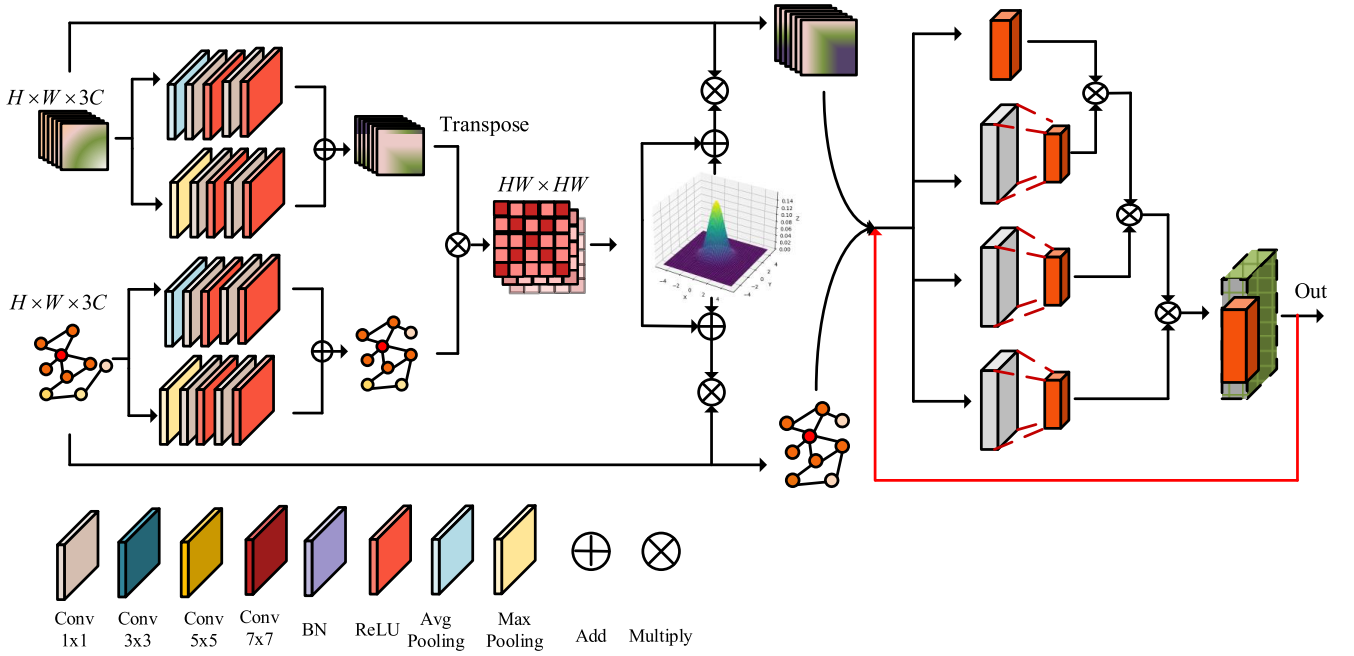


Fig. 4. Structural block diagram of GWFM.

process is

$$Q_{i,j} = \begin{cases} 1, & \hat{X}_i \text{ in } S_j \\ 0, & \hat{X}_i \notin S_j \end{cases} \quad (13)$$

$$\hat{X} = \text{flatten}(X). \quad (14)$$

\hat{X} in $\mathbb{R}^{HW \times B}$ is the data obtained by flattening the two spatial dimensions of the original HSI data. $Q_{i,j}$ represents the relationship between the i th pixel and the j th superpixel S_j . The conversion process between graph nodes and superpixels can be represented as

$$H = \text{Encoder}(X; Q) = \bar{Q}^T \text{flatten}(X) \quad (15)$$

$$\tilde{X} = \text{Decoder}(H; Q) = \text{reshape}(QH). \quad (16)$$

Among them, \bar{Q} represents the normalized Q of the column, and H is a graph node composed of superpixels. $\text{reshape}(\cdot)$ represents the spatial dimension of the restored flattened data. $\text{Encode}(\cdot)$ represents the mapping from pixels to graph nodes, and $\text{Decode}(\cdot)$ represents the mapping from graph nodes to pixels. In GWFM, first, the input CNN features and GCN features are, respectively, weighted with channel attention. The process can be represented as

$$X_{\text{Avg}} = \delta(W_{1 \times 1} \times (\delta(W_{1 \times 1} \times \text{Avg}(X_{\text{in}}) + b)) + b) \quad (17)$$

$$X_{\text{Max}} = \delta(W_{1 \times 1} \times (\delta(W_{1 \times 1} \times \text{Max}(X_{\text{in}}) + b)) + b) \quad (18)$$

$$X_{\text{out}} = X_{\text{Avg}} + X_{\text{Max}}. \quad (19)$$

Among them, $W_{1 \times 1}$ represent 2-D convolutional weights of size 1×1 .

After channel attention weighting, the convolutional features are transposed and cross-multiplied with the graph convolutional features to obtain a spatial attention weight matrix. In order to better suppress unimportant features and highlight important and subimportant features. The spatial attention weight matrix after cross multiplication is subjected to a

2-D Gaussian mapping by GWFM, and the mapped features are input into a feedback high-order gated convolution for forward propagation. Feedback recursive gated convolution can achieve high-order information exchange through gated convolution, and the representational ability of the model is improved. By using a feedback mechanism, the features extracted from recursive-gated convolution are fed back to the input features in an attention weighted manner, thereby achieving rectification of the input features. The calculation process can be expressed as

$$\text{Gaussian}(x_1, x_2) = \frac{1}{\sqrt{2\pi}\theta_1\theta_2} e^{-\frac{[\theta_2^2(x_1-u_1)^2 + \theta_1^2(x_2-u_2)^2]}{2\theta_1^2\theta_2^2}} \quad (20)$$

$$x_{\text{gout}} = \text{Gaussian}(x_{\text{col}}, x_{\text{row}}) + x_{\text{in}} \quad (21)$$

$$[p_0, q_1, q_2, \dots, q_{n-1}] = \vartheta(x_{\text{gout}}) \quad (22)$$

$$Fg^n \text{Conv} = f_k(q_k) \odot g_k(p_k) / \alpha. \quad (23)$$

Among them, x_{col} and x_{row} represent spatial column features and spatial row features, respectively. $\vartheta(\cdot)$ represents the mapping function. $p_0, q_1, q_2, \dots, q_{n-1}$ is a feature mapped from $\vartheta(\cdot)$. $f_k(\cdot)$ represents depthwise separable convolution, $g_k(\cdot)$ represents point convolution. \odot represents dot product, α represents scaling factor.

D. Implementation Process

Taking the Indian Pines dataset as an example, the implementation process of MRSGFN is described as follows. First, the input HS data $X \in \mathbb{R}^{H \times W \times B}$ is segmented by SLIC algorithm to obtain the transformation matrix $Q \in \mathbb{R}^{H \times W \times N}$, node matrix $H \in \mathbb{R}^{N \times C}$, and adjacency matrix $A \in \mathbb{R}^{N \times N}$. Then, the node matrix H and adjacency matrix A are input into the graph convolution branch to extract graph features. In the graph convolution branch, MHRA is utilized in an

attention-weighted manner to expand the receptive field of graph convolution. The inputs of MHRA are node matrix H , adjacency matrix A , and K -order hop graph adjacency matrix A_k . MHRA first performs graph feature extraction on input H and A to obtain node feature H_1 . Then, H_1 performs graph convolution mapping with A_k and A respectively, obtaining three feature vectors of Q , K , V . Then Q and K perform vector dot multiplication to obtain the attention matrix, and finally the attention matrix is weighted and multiplied with V .

In the convolutional branch, the input data are $X \in \mathbb{R}^{H \times W \times B}$. First, SI2FEM is utilized to group spectral features, and the grouped data are represented as $X_g \in \mathbb{R}^{H \times W \times n \times G}$. Then, the grouped features are sequentially subjected to intragroup and intergroup feature extraction and dimensionality reduction. Finally, the features extracted by the two branches are input into GWFM for 2-D Gaussian mapping weighting, and the data are sent to feedback recursive gated convolution for forward propagation. The implementation details of the MRSGFN method are described in Algorithm 2.

Algorithm 2 Implementation details of the MRSGFN method

Input: HSIs data $X \in \mathbb{R}^{H \times W \times B}$, landmark label $Y \in \mathbb{R}^{h \times w}$, PCA band number $b = 3$ training sample ratio $q\%$.

Output: Predictive labels for the dataset.

- 1: Set the batch size to 64 and the learning rate lr of optimizer Adam to $5e-4$. Training round $T = 200$, superpixel segmentation parameter $S = 100$.
 - 2: Divide the training sample set according to the proportion of $q\%$, and the testing sample set according to $1-q\%$.
 - 3: for $i = 1$ to T do
 - 4: The input data is executed using the SLIC algorithm to obtain the transformation matrix $Q \in \mathbb{R}^{H \times W \times N}$, node matrix $H \in \mathbb{R}^{N \times C}$, and adjacency matrix $A \in \mathbb{R}^{N \times N}$.
 - 5: The node matrix H and adjacency matrix A are inputted into the MHRA of the graph convolution branch to obtain the graph node feature matrix $H_{out} \in \mathbb{R}^{N \times C}$.
 - 6: $X \in \mathbb{R}^{H \times W \times B}$ is input into the convolutional branch and SI2FEM is executed.
 - 7: The features extracted from graph convolution and convolutional branches are input into GWFM for 2-D Gaussian weighted fusion.
 - 8: The convolutional integral branch feature and the convolutional integral branch feature are cascaded to obtain X_{cls} in $\mathbb{R}^{H \times W \times 6C}$.
 - 9: The linear layer outputs the predicted category of pixels.
- end for

III. EXPERIMENTAL RESULTS AND ANALYSIS

In this article, extensive experiments have been conducted on three common datasets to evaluate the effectiveness of the proposed MRSGFN method. The classification performance of the proposed method is compared with that of other advanced methods from multiple perspectives. The experimental results validate the effectiveness of the proposed method. The dataset

TABLE I
CATEGORY NAMES AND NUMBER OF DATA SAMPLE DIVISIONS FOR THE INDIAN PINES DATASET

| Category | Label color | Land cover | Training | Total |
|----------|---|-------------------------|----------|-------|
| 1 |  | Alfalfa | 1 | 46 |
| 2 |  | Corn-notill | 29 | 1428 |
| 3 |  | Corn-mintill | 17 | 830 |
| 4 |  | Corn | 5 | 237 |
| 5 |  | Grass-pasture | 10 | 483 |
| 6 |  | Grass-trees | 15 | 730 |
| 7 |  | Grass-pasture-mowed | 1 | 28 |
| 8 |  | Hay-windrowed | 10 | 478 |
| 9 |  | Oats | 1 | 20 |
| 10 |  | Soybean-notill | 20 | 972 |
| 11 |  | Soybean-mintill | 50 | 2455 |
| 12 |  | Soybean-clean | 12 | 593 |
| 13 |  | Wheat | 5 | 205 |
| 14 |  | Woods | 26 | 1265 |
| 15 |  | Bldg-Grass-Tree-Drivers | 8 | 386 |
| 16 |  | Stone-Steel-Towers | 2 | 93 |
| Total | / | / | 212 | 10249 |

TABLE II
CATEGORY NAMES AND NUMBER OF DATA SAMPLE PARTITIONS FOR THE PAVIA DATASET

| Category | Label color | Land cover | Training | Total |
|----------|---|----------------------|----------|-------|
| 1 |  | Asphalt | 14 | 6631 |
| 2 |  | Meadows | 38 | 18649 |
| 3 |  | Gravel | 5 | 2099 |
| 4 |  | Trees | 7 | 3064 |
| 5 |  | Painted metal sheets | 3 | 1345 |
| 6 |  | Bare Soil | 11 | 5029 |
| 7 |  | Bitumen | 3 | 1330 |
| 8 |  | Self-Blocking Bricks | 8 | 3682 |
| 9 |  | Shadows | 2 | 947 |
| Total | / | / | 91 | 42776 |

used in the experiment includes the Indian Pines dataset, Pavia dataset, and Salinas dataset.

A. Dataset Description

Indian Pines dataset: HSIs data are captured by AVIRIS sensors. A total of 21,025 pixels and 224 spectral reflection bands are included, and after filtering out the water absorption band and low signal-to-noise ratio band, the HSIs data contains 200 spectral bands. The Indian Pines landscape includes two-third agriculture and one-third forest or other vegetation. The names and sample divisions of each category in the dataset are shown in Table I.

Pavia dataset: Pavia data are captured by ROSIS-3 sensors, in which nine ground cover species are included. The image space size is 610×340 and contains 115 spectral bands in the wavelength range from 0.43 to $0.89 \mu\text{m}$, with 103 spectral bands remaining after the absorbing bands and the low signal-to-noise bands are removed. The names and sample divisions of each category in the dataset are shown in Table II.

Salinas dataset: the AVIRIS sensor captured HSIs data from the Salinas Valley in California. The image space size is 512×217 and contains 224 spectral bands, with 200 spectral bands remaining after the noise bands have been removed. Salinas has a spatial resolution of 3.7 m and contains 16 crop

categories. The names and sample divisions of each category in the dataset are shown in Table III.

B. Experimental Setup

All experiments in this article were done on a platform with an Intel¹ Core² i9-9900K CPU, an NVIDIA GeForce RTX 3090Ti GPU, and 128 G of random access memory, using the language framework Pytorch. In this article, three common evaluation indicators are chosen to evaluate the classification performance of the model, namely overall accuracy (OA), average accuracy (AA), and Kappa coefficient. OA represents the ratio of the number of correctly categorized samples to the total number of samples. AA represents the average of the classification accuracy for each category. Kappa coefficient is the evaluation metric that has been used to measure the robustness of the model.

To verify the effectiveness of the MRSGFN method proposed in this article, multiple advanced networks based on CNNs, transformers, and GCNs were selected. This includes HybridSN [41], A2S2K-ResNet [24], FECNet [24], SSFTT [28], CTMixer [42], CNN-enhanced GCN (CEGCN) [40], FDGC [37], and AMGCFN [38]. HybridSN is a CNN network that combines 2DCNN and 3DCNN. A2S2K-ResNet improves the residual network through adaptive spectral space convolution kernels and employs an effective feature recalibration mechanism to improve classification performance. FECNet constructs dilated convolution blocks through 3-D dilated convolution, and the receptive field of the convolution is expanded without increasing computational complexity. SSFTT and CTMixer are transformer-based classification methods that have a global receptive field, and low-frequency features of images can be better extracted for image classification. CEGCN, FDGC, WFCG, and AMGCFN are GCN-based methods. CEGCN fully utilizes the advantages of CNN and GCN, extracting features from small-scale and regular target area HSI data using CNN, and extracting features from large-scale and irregularly shaped HSI data using GCN. Unlike CEGCN, FDGC can adaptively capture the topology information of a graph in a supervised manner. AMGCFN designed a cross attention fusion module to adaptively fuse the features of two subnetworks.

C. Model Analysis

1) *Ablation Analysis*: The method proposed in this article mainly consists of three modules, namely GWFM, SI2FEM, and MHRA. In order to better validate the effectiveness of each module of the proposed MRSGFN method, the performance of different module combinations is compared to demonstrate the effectiveness of each module. Some ablation experiments were conducted on three commonly used datasets. The experimental results are shown in Table IV. In Table IV, “√” indicates that the module is adopted in the current module combination, and “–” indicates that the module is not adopted in the module combination. There are four module combinations in

¹Registered trademark.

²Trademarked.

TABLE III
CATEGORY NAMES AND NUMBER OF DATA SAMPLE PARTITIONS FOR THE SALINAS DATASET

| Category | Label color | Land cover | Training | Total |
|----------|---|---------------------------|----------|-------|
| 1 |  | Broccoli-green-weeds_1 | 5 | 2009 |
| 2 |  | Broccoli-green-weeds_2 | 8 | 3726 |
| 3 |  | Fallow | 4 | 1976 |
| 4 |  | Fallow-rough-plow | 3 | 1394 |
| 5 |  | Fallow-smooth | 6 | 2678 |
| 6 |  | Stubble | 8 | 3959 |
| 7 |  | Celery | 8 | 3579 |
| 8 |  | Grapes-untrained | 23 | 11271 |
| 9 |  | Soil-vinyard-develop | 13 | 6203 |
| 10 |  | Corn-senesced-green-weeds | 7 | 3278 |
| 11 |  | Lettuce-romaine-4wk | 3 | 1068 |
| 12 |  | Lettuce-romaine-5wk | 4 | 1927 |
| 13 |  | Lettuce-romaine-6wk | 2 | 916 |
| 14 |  | Lettuce-romaine-7wk | 3 | 1070 |
| 15 |  | Vinyard-untrained | 15 | 7268 |
| 16 |  | Vinyard-vertical-trellis | 4 | 1807 |
| Total | / | / | 116 | 54129 |

TABLE IV
IMPACT OF DIFFERENT MODULES ON OA VALUES OF THREE DATASETS

| Case | Component | | | DataSets | | |
|------|-----------|--------|------|--------------|--------------|--------------|
| | GWFM | SI2FEM | MHRA | Indian Pines | Pavia | Salinas |
| 1 | √ | – | – | 93.37 | 95.94 | 95.03 |
| 2 | √ | √ | – | 93.76 | 96.47 | 95.70 |
| 3 | √ | – | √ | 94.26 | 96.71 | 96.06 |
| 4 | √ | √ | √ | 94.98 | 97.17 | 96.73 |

MRSGFN. From Table IV, it can be seen that in Case 1, only the GWFM module is adopted in the network, and the OAs on three datasets are all the lowest. In Case 2, GWFM module and SI2FEM module are adopted in the network. It can be seen that the OAs obtained in Case 2 on three datasets are all higher than that obtained in Case 1. Especially for the Salinas dataset, the OA of Case 2 is nearly 0.7% higher than that of Case 1. Case 3 includes two modules: GWFM and MHRA. It can be seen that for all three datasets, the OAs of Case 3 are higher than those of Case 1, and the increase in accuracy at this time is greater than that of Case 2. This indicates that the increase in receptive field has a significant impact on classification results. Case 4 is the final state of the network, which includes three modules: GWFM, SI2FEM, and MHRA. At this point, the OAs on the three datasets are the highest among all module combinations. Specifically, compared to the classification accuracy of Case 1, Case 2, and Case 3, Case 4 has the largest increase in OA on the Indian Pines dataset.

To further demonstrate the effectiveness of GWFM, some ablation experiments were conducted on different datasets. The results of the ablation experiment are shown in Table V, where A represents the Gaussian weighted attention module in GWFM and B represents the feedback recursive gated convolution module in GWFM. “√” indicates that the module is adopted, and “–” indicates that the module is not adopted. First, from the comparison of Case 1 and Case 3 in Table V,

TABLE V
IMPACT OF GWFM ON OA VALUES

| Case | Without GWFM | With GWFM | | DataSets | | |
|------|--------------|-----------|---|--------------|--------------|--------------|
| | | A | B | Indian Pines | Pavia | Salinas |
| 1 | √ | — | — | 19.19 | 45.38 | 40.66 |
| 2 | — | √ | — | 89.46 | 94.79 | 95.23 |
| 3 | — | √ | √ | 94.98 | 97.17 | 96.73 |

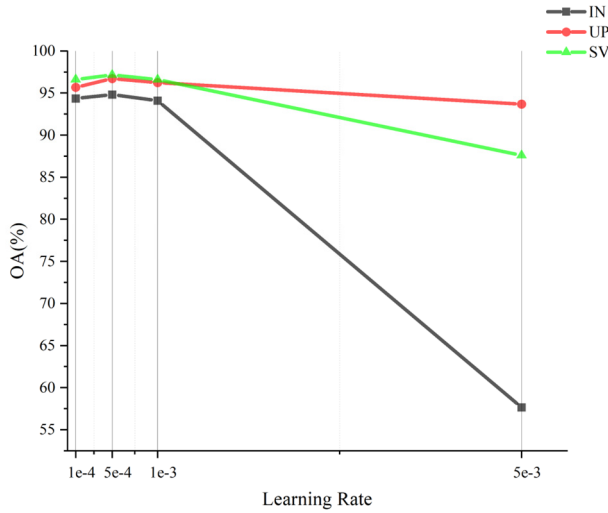


Fig. 5. Impact of learning rate on classification accuracy on different datasets.

it can be found that GWFM can fully fuse the features extracted by the two subnetworks, thereby obtaining satisfactory classification results. However, without using GWFM to fuse the features extracted by the two subnetworks, the classification results of the network are very poor. Specifically, for the Indian Pines dataset, without using GWFM to fuse the features extracted by two sub networks, the overall classification accuracy of the network is only 19.19%. By comparing the OAs of Case 2 and Case 3 on three different datasets, it is obvious that GWFM with Gaussian weighted attention module can significantly improve the classification accuracy of all three datasets, which fully demonstrates the importance of feedback recursive gated convolution in GWFM.

2) *Parameter Sensitivity Analysis*: During the training process, different learning rates have a significant impact on the classification performance of the model. In order to select the optimal learning rate for the proposed MRSGFN method, some experiments using different learning rates were conducted on three datasets. The selected learning rate is $\{1e-4, 5e-4, 1e-3, 5e-3\}$, and the experimental results are shown in Fig. 5. From Fig. 5, it can be seen that on the three datasets, as the learning rate increases, OA shows a trend of first increasing and then decreasing. When the change in learning rate is small, the classification performance of the network is less affected. For example, when the learning rate changes from $1e-4$ to $5e-4$, the classification performance of the model is less affected. When the learning rate changes from $1e-3$ to $5e-3$, the classification performance of the model is greatly affected. Specifically, for the Indian Pines dataset, the classification performance of the model changes dramatically

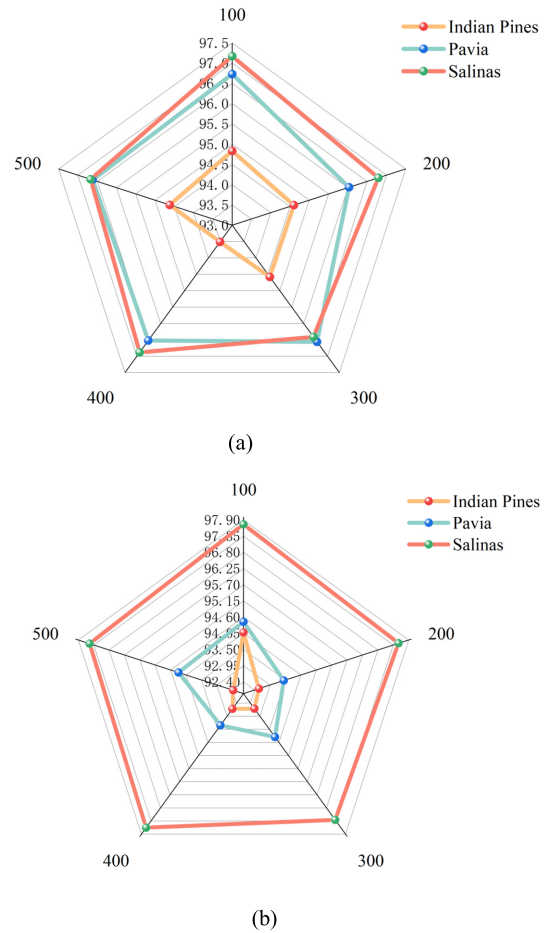
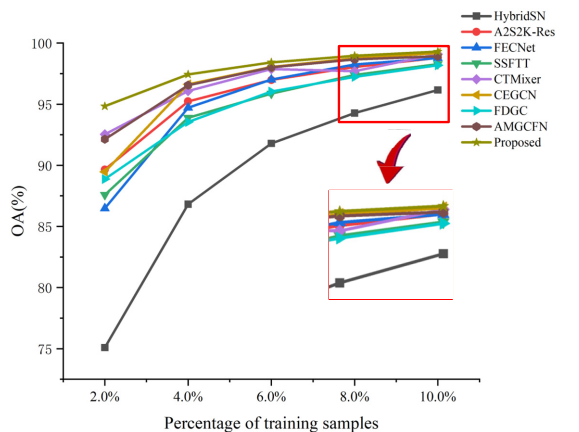


Fig. 6. Impact of different superpixel segmentation scales on classification accuracy. Impact of different superpixel segmentation scales on (a) OA value and (b) AA value.

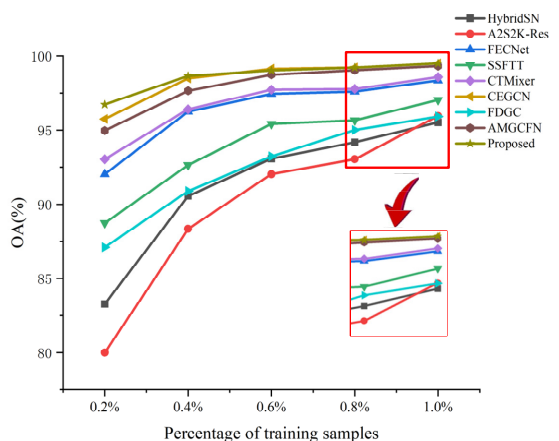
when the learning rate changes from $1e-3$ to $5e-3$. From Fig. 5, it can be observed that for all three datasets, the impact of learning rate on network classification performance shows a trend of first increasing and then decreasing. When the learning rate is $5e-4$, the classification performance of the network is the best; therefore, $5e-4$ is chosen as the learning rate.

3) *Superpixel Segmentation Scale*: The conversion of HSIs image data into graph-structured data requires superpixel segmentation. However, different segmentation scales have different impacts on classification accuracy. In order to select the optimal superpixel segmentation scale, some experiments with different segmentation scales were conducted on three different datasets. The superpixel segmentation scale is $\{100, 200, 300, 400, 500\}$, and the experimental results are shown in Fig. 6.

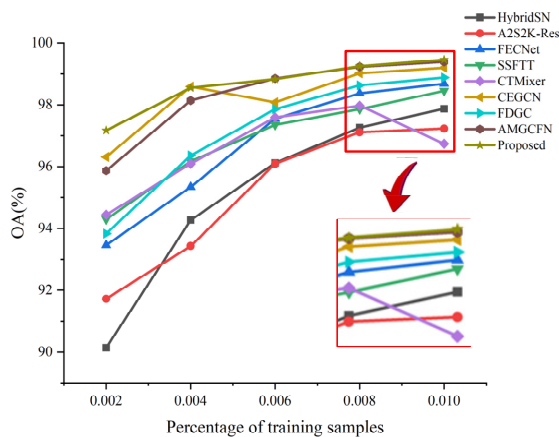
From Fig. 6(a), it can be seen that the Salinas dataset are not very sensitive to changes in superpixel segmentation scale. This is because the Salinas dataset has large land cover targets, and changes in superpixel scale do not have a significant impact on Salinas classification results. In Fig. 6(b), the AA reflects the average classification accuracy of each subcategory. There are small ground cover targets in the Pavia and Indian Pines datasets, and large-scale superpixel



(a)



(b)



(c)

Fig. 7. Impact of different training sample ratios on OA. Impact of OA on (a) Indian Pines dataset, (b) OA in the Pavia dataset, and (c) Salinas dataset.

segmentation will generate sparse superpixel blocks, which will cover more small targets. Therefore, for the Pavia and Indian Pines datasets, as the segmentation scale increases, the average classification accuracy will show a decreasing trend, which is shown in Fig. 6(b). Specifically, for the Indian Pines dataset, the average classification accuracy has significantly

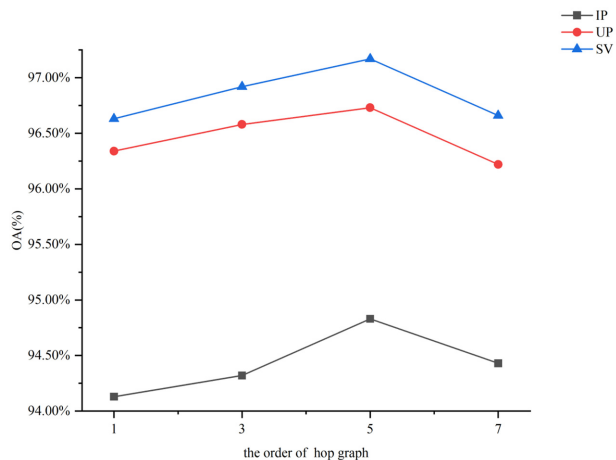


Fig. 8. Impact of different order of hop graph on OA.

decreased due to the dense distribution of land cover in the dataset. Many different types of land cover are in the same area, and large-scale superpixel segmentation can result in a superpixel containing multiple different types of land cover. From Fig. 6, it can be seen that the three different datasets can achieve optimal results for both OA and AA when the superpixel segmentation scale is 100; therefore, we choose 100 as the superpixel segmentation scale.

4) *Different Training Sample Ratios:* The cost of annotating HSIs data is expensive, so the training samples for HSIs are usually limited. In the above experiments, a large number of experiments have demonstrated the excellent performance of the proposed MRSGFN method in small samples. In this part, the classification performance of MRSGFN and all comparison methods has been validated on three datasets under different training sample ratios. Among them, the sample ratio of the Indian Pines dataset is selected as {2%, 4%, 6%, 8%, 10%}, and the sample ratio of the Pavia and Salinas datasets is selected as {0.2%, 0.4%, 0.6%, 0.8%, 1.0%}. The impact of different training sample ratios on OA is shown in Fig. 7. From Fig. 7, it can be seen that as the proportion of training samples increases, the OA values of most comparison methods show an increasing trend. For the maximum training sample ratio, the highest OA values are obtained. The method proposed in this article always maintains the best classification performance under all training sample ratios. On the contrary, as the proportion of training samples decreases, the classification performance of all methods decreases to a certain extent. Specifically, in the Indian Pines dataset, the greatest decrease in classification accuracy occurs when the training ratio is reduced from 4% to 2%. Similarly, in the Pavia and Salinas datasets, the greatest decrease in classification accuracy occurs when the training ratio is reduced from 0.4% to 0.2%. When the proportion of training samples is small, the method proposed in this article still has excellent classification performance. These indicate that the robustness of the proposed MRSGFN method is very satisfactory under different training sample ratios.

5) *Different Order of Hop Graph:* To better illustrate the impact of hop graph order on model performance, some

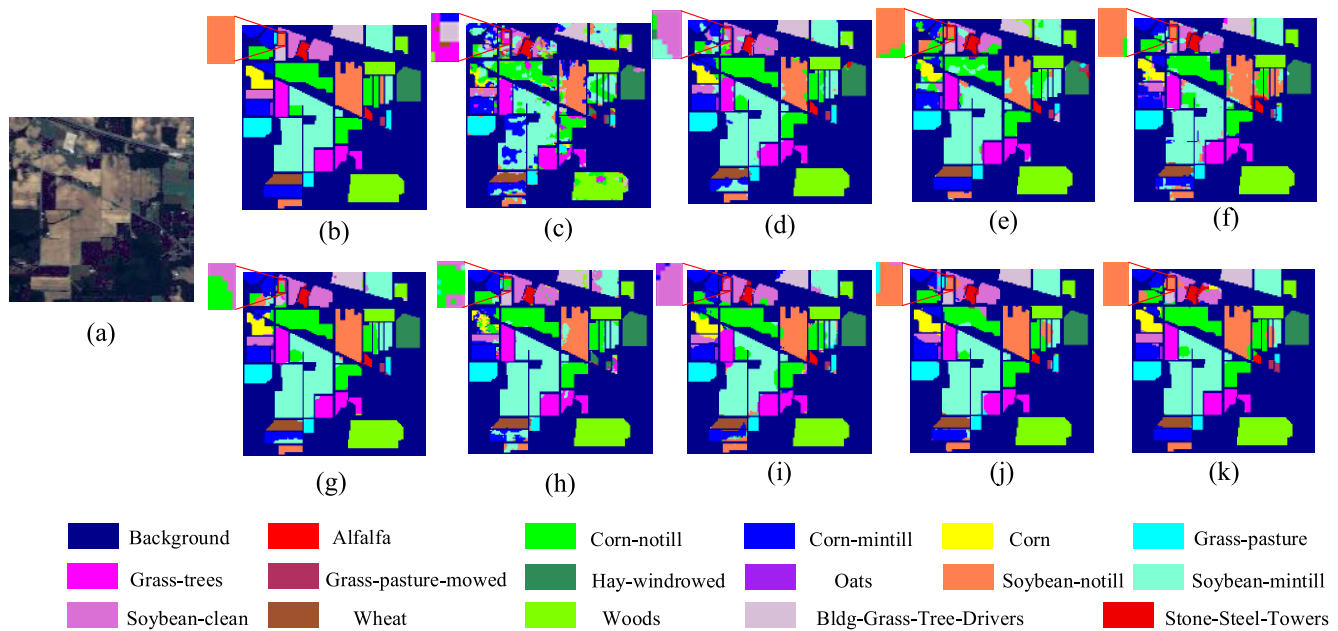


Fig. 9. Classification maps obtained by all methods on the Indian Pines dataset. (a) Pseudo color map, (b) real feature map, (c) HybridSN, (d) A2S2K-ResNet, (e) FECNet, (f) and (g) SSFTT and CTMixer, respectively, (h)–(j) CEGCN, FDGC, and AMGCFN, and (k) MRSGFN.

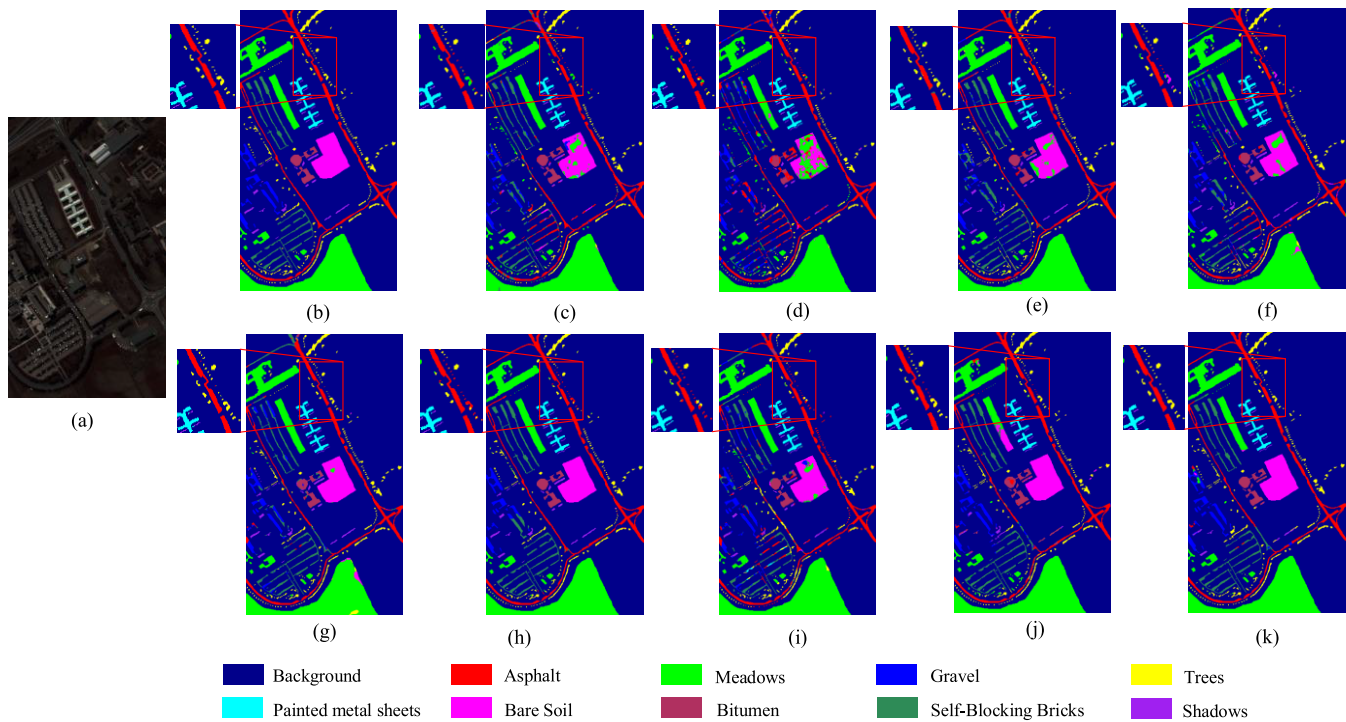


Fig. 10. Classification maps obtained by all methods on the Pavia dataset. (a) Pseudo color map, (b) real feature map, (c) HybridSN, (d) A2S2K-ResNet, (e) FECNet, (f) and (g) SSFTT and CTMixer, respectively, (h)–(j) CEGCN, FDGC, and AMGCFN, and (k) MRSGFN.

experiments were conducted on three different datasets, that is, Indian Pines, Pavia, and Salinas, using different order of hop graph. The order range of hop graph is $\{1, 3, 5, 7\}$, and the experimental results are shown in Fig. 8. From Fig. 8, it can be seen that for the Indian Pines data, as the hop order increases, the OA value of the model shows a trend of first increasing and then decreasing, and reaches its maximum value when the hop order is 5. Similarly, for the Salinas and Pavia datasets, OA also showed a trend of first increasing

and then decreasing. This is because as the order of the hop graph increases, the receptive field of graph convolution also gradually increases. However, when the receptive field is large, not only it requires more data preprocessing time but the large receptive field also prevents the model from paying attention to local information, resulting in the loss of important local information and a decrease in the model’s classification performance. In summary, the order of hop graphs selected in this article is 5.

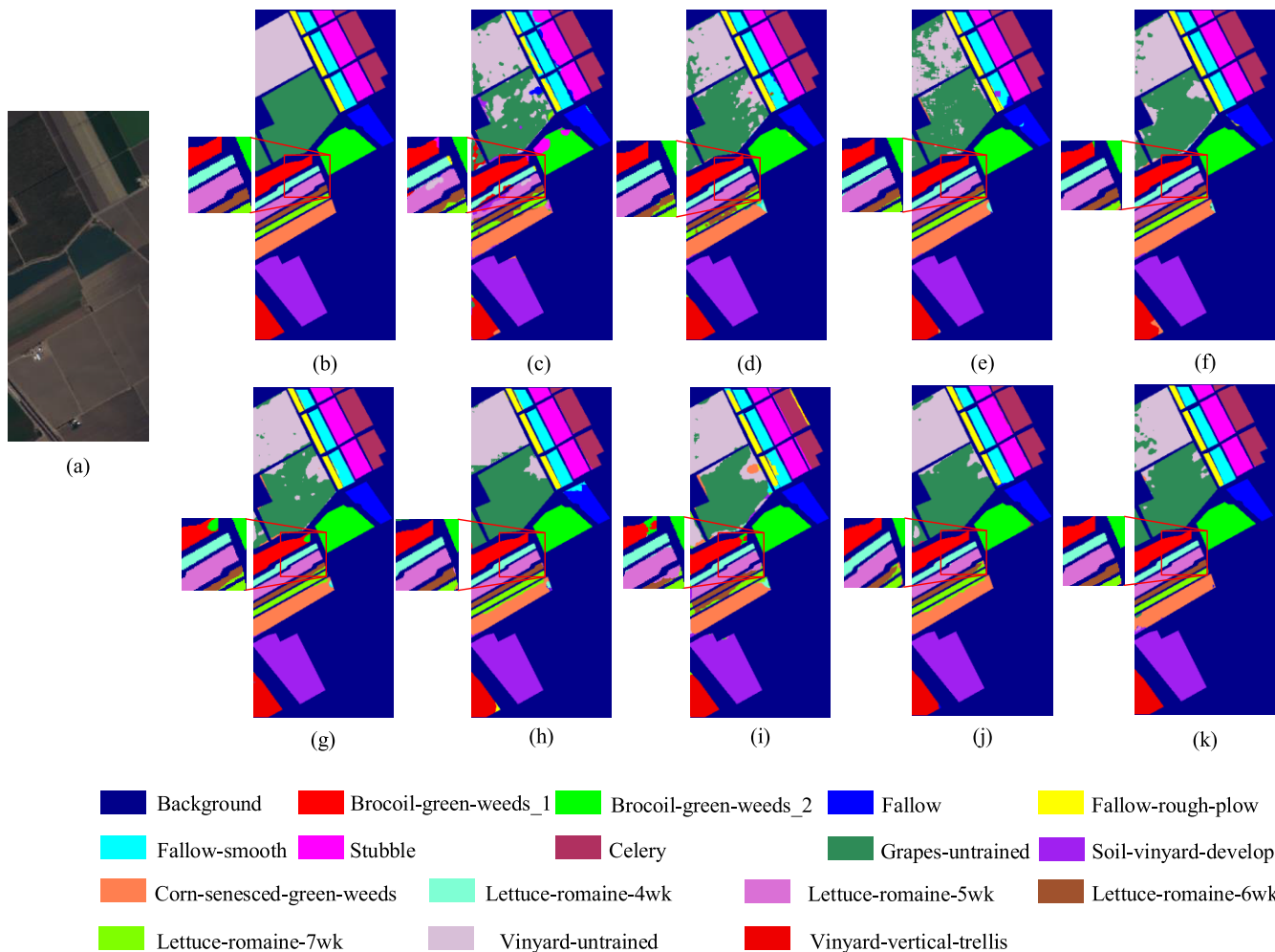


Fig. 11. Classification maps obtained by all methods on the Salinas dataset. (a) Pseudo color map, (b) real feature map, (c) HybridSN, (d) A2S2K-ResNet, (e) FECNet, (f) and (g) SSFTT and CTMixer, respectively, (h)–(j) CEGCN, FDGC, and AMGCFN, and (k) MRSGFN.

D. Analysis of Results

1) *Quantitative Analysis*: Tables VI–VIII show the OA, AA, Kappa, and classification accuracy for each category of all methods in this article on the Indian Pines, Pavia, and Salinas datasets. The best classification results have been bolded. From Tables VI–VIII, it can be seen that both transformer-based and CNN-based methods achieve poor classification accuracy in the case of a small number of samples, as these methods are modeled under a large number of training samples. In GCN-based methods, AMGCFN benefits from its cascaded multihop graph structure, which enables it to obtain richer graph features. Therefore, the classification performance of AMGCFN exceeds that of other comparison methods, but it still performs worse than the classification performance of the proposed MRSGFN method. From Tables VI–VIII, it can be seen that the OA, AA, and Kappa values of the MRSGFN method proposed in this article are optimal on all datasets. For the Indian Pines dataset, compared to other comparison methods, the proposed MRSGFN method achieved the best classification results for nine land cover categories. Specifically, the classification accuracy of category 9 “Oats” reached 100%. For the Pavia dataset, compared to other comparison methods, the proposed MRSGFN method achieved the highest

classification accuracy for four land cover categories. From the data in Table VIII, it can be observed that compared to other comparison methods, the proposed MRSGFN method achieved the best classification results for a total of eight land cover categories. Specifically, the classification results for the second and ninth categories in the Salinas dataset reached 100%. Even compared to the classification results of category 1 and category 7 in Salinas data, the proposed MRSGFN method has only 0.08% and 0.04% lower OA than the optimal classification results.

2) *Visual Assessment*: In order to provide a more intuitive analysis of the classification performance of the proposed method on different datasets, visual analysis was conducted on the classification results of all methods. Figs. 9–11 show the visualize classification results of all methods on the Indian Pines, Pavia, and Salinas datasets, respectively. From Figs. 9–11, it can be seen that compared with other methods, the proposed MRSGFN method can provide classification results that are closer to the real image. The comparison method based on CNNs and the comparison method based on transformer exhibit a significant amount of noise on all three datasets, as these methods are based on a large number of training samples for classification. Specifically, for example,

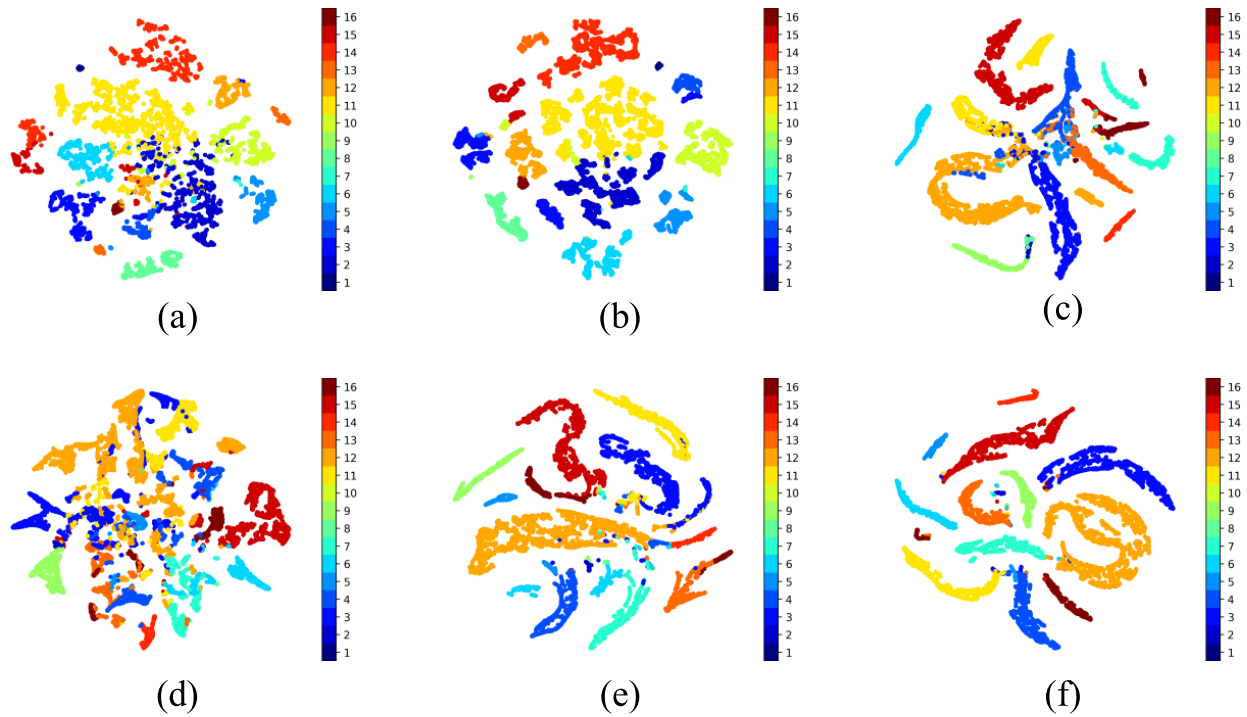


Fig. 12. Comparison of t-SNE visualization results on the Indian Pines dataset. (a)–(f) Visualization results of t-SNE for FECNet, CTMixer, CEGCN, FDGC, AMGCFN, and MRSGFN, respectively.

TABLE VI
CLASSIFICATION RESULTS OF DIFFERENT METHODS ON THE INDIAN PINES DATASET

| Method | CNN | | | Transformer | | GCN | | | |
|-----------|----------|-----------|--------|-------------|--------------|--------------|-------|--------------|---------------|
| | HybridSN | A2S2K-Res | FECNet | SSFTT | CTMixer | CEGCN | FDGC | AMGCFN | Proposed |
| OA (%) | 75.09 | 89.65 | 86.48 | 87.59 | 92.54 | 89.46 | 88.87 | 92.13 | 94.83 |
| AA (%) | 71.67 | 87.83 | 81.50 | 85.50 | 89.52 | 74.12 | 81.61 | 90.57 | 94.08 |
| Kappa (%) | 71.51 | 88.13 | 84.56 | 85.79 | 91.49 | 87.88 | 85.03 | 91.04 | 94.10 |
| 1 | 65.83 | 85.22 | 65.09 | 85.98 | 89.26 | 7.27 | 75.69 | 71.63 | 87.44 |
| 2 | 67.50 | 87.29 | 85.07 | 83.31 | 89.85 | 87.26 | 73.61 | 87.53 | 93.86 |
| 3 | 64.00 | 88.55 | 81.28 | 82.08 | 91.72 | 75.56 | 74.43 | 92.04 | 92.60 |
| 4 | 66.50 | 93.45 | 80.00 | 90.00 | 92.08 | 49.16 | 75.40 | 92.19 | 95.91 |
| 5 | 87.27 | 97.74 | 95.47 | 93.51 | 97.25 | 87.82 | 79.75 | 85.35 | 89.57 |
| 6 | 85.86 | 96.97 | 92.62 | 95.77 | 95.18 | 99.26 | 86.41 | 94.51 | 97.78 |
| 7 | 46.44 | 75.73 | 62.30 | 59.29 | 68.35 | 46.54 | 52.60 | 88.24 | 90.66 |
| 8 | 92.24 | 99.59 | 99.04 | 99.31 | 99.37 | 98.60 | 89.71 | 99.70 | 99.80 |
| 9 | 37.86 | 49.49 | 41.35 | 61.68 | 70.22 | 17.22 | 42.02 | 97.37 | 100.00 |
| 10 | 68.17 | 88.55 | 81.10 | 84.12 | 88.70 | 89.01 | 75.43 | 88.06 | 89.31 |
| 11 | 77.40 | 84.71 | 86.36 | 85.63 | 93.55 | 96.31 | 81.97 | 96.22 | 96.78 |
| 12 | 65.33 | 89.65 | 80.10 | 86.21 | 90.69 | 77.57 | 66.51 | 81.75 | 90.45 |
| 13 | 91.40 | 94.31 | 92.14 | 97.18 | 95.94 | 98.97 | 78.96 | 94.99 | 98.51 |
| 14 | 86.52 | 95.16 | 94.64 | 94.45 | 96.55 | 99.02 | 86.47 | 95.78 | 98.26 |
| 15 | 73.54 | 91.19 | 85.74 | 87.51 | 89.70 | 75.16 | 70.66 | 93.61 | 94.57 |
| 16 | 70.84 | 87.76 | 81.71 | 81.98 | 83.93 | 79.10 | 65.56 | 90.20 | 89.71 |

the HybridSN method is a hybrid classification network based on 2DCNN and 3DCNN, which requires a large number of samples for training to extract discriminative features from images. However, in the case of small samples, the feature extraction ability of CNN is limited, and satisfactory features cannot be extracted for classification. Under a small number of training samples, the classification results based on graph

convolution methods are more satisfactory than those based on CNN and transformer methods. Specifically, for the Indian Pines and Pavia datasets, the classification maps obtained by GCN-based methods have less noise. This is because Indian Pines and Pavia have more land cover for small targets in their data. Graph convolution can fully consider the spatial relationship between objects, and better extract local features

TABLE VII
CLASSIFICATION RESULTS OF DIFFERENT METHODS ON THE PAVIA DATASET

| Method | CNN | | | Transformer | | GCN | | | |
|-----------|----------|-----------|--------------|-------------|--------------|--------------|-------|--------------|--------------|
| | HybridSN | A2S2K-Res | FECNet | SSFTT | CTMixer | CEGCN | FDGC | AMGCFN | Proposed |
| OA (%) | 83.28 | 80.00 | 92.03 | 88.74 | 93.04 | 95.75 | 87.10 | 94.97 | 96.73 |
| AA (%) | 79.19 | 81.61 | 89.23 | 87.02 | 90.25 | 91.11 | 80.49 | 90.66 | 94.00 |
| Kappa (%) | 77.63 | 72.54 | 89.44 | 84.96 | 90.76 | 94.36 | 82.83 | 93.33 | 95.66 |
| 1 | 79.92 | 70.78 | 93.09 | 87.86 | 92.81 | 97.97 | 70.48 | 92.20 | 96.69 |
| 2 | 92.12 | 84.76 | 97.54 | 93.54 | 97.88 | 98.62 | 87.23 | 98.79 | 98.90 |
| 3 | 62.72 | 73.83 | 69.07 | 72.20 | 74.75 | 85.04 | 64.24 | 85.05 | 84.45 |
| 4 | 81.22 | 93.56 | 93.70 | 94.64 | 96.53 | 89.37 | 69.19 | 86.91 | 90.90 |
| 5 | 94.40 | 98.06 | 98.91 | 96.92 | 98.23 | 99.96 | 83.86 | 98.89 | 99.87 |
| 6 | 86.65 | 84.53 | 94.95 | 88.43 | 96.01 | 98.13 | 84.98 | 98.46 | 98.83 |
| 7 | 76.35 | 85.04 | 86.88 | 89.68 | 86.66 | 85.56 | 77.59 | 93.86 | 95.89 |
| 8 | 57.97 | 58.02 | 73.94 | 70.80 | 78.18 | 93.60 | 62.77 | 94.21 | 97.52 |
| 9 | 81.39 | 85.88 | 97.01 | 89.05 | 91.28 | 71.75 | 51.60 | 67.62 | 82.92 |

TABLE VIII
CLASSIFICATION RESULTS OF DIFFERENT METHODS ON THE SALINAS DATASET

| Method | CNN | | | Transformer | | GCN | | | |
|-----------|----------|-----------|--------------|--------------|--------------|---------------|-------|---------------|---------------|
| | HybridSN | A2S2K-Res | FECNet | SSFTT | CTMixer | CEGCN | FDGC | AMGCFN | Proposed |
| OA (%) | 90.14 | 91.72 | 93.46 | 94.29 | 94.44 | 96.43 | 93.83 | 95.87 | 97.17 |
| AA (%) | 89.99 | 94.94 | 95.98 | 95.98 | 96.54 | 97.08 | 93.24 | 96.08 | 97.75 |
| Kappa (%) | 89.03 | 90.79 | 92.71 | 93.64 | 93.83 | 96.02 | 93.14 | 95.40 | 96.84 |
| 1 | 92.25 | 99.34 | 99.33 | 99.67 | 96.75 | 99.58 | 87.92 | 99.53 | 99.59 |
| 2 | 97.55 | 99.76 | 99.77 | 99.57 | 99.64 | 100.00 | 89.59 | 99.41 | 100.00 |
| 3 | 93.85 | 96.45 | 96.13 | 99.58 | 98.56 | 96.00 | 83.44 | 99.27 | 94.22 |
| 4 | 83.97 | 95.29 | 92.89 | 96.42 | 92.21 | 98.19 | 80.16 | 95.88 | 98.24 |
| 5 | 85.67 | 96.34 | 97.65 | 96.27 | 99.10 | 97.82 | 82.78 | 93.78 | 95.03 |
| 6 | 94.86 | 99.72 | 99.63 | 99.07 | 99.00 | 99.82 | 88.06 | 99.24 | 99.92 |
| 7 | 97.01 | 99.64 | 99.53 | 99.43 | 99.69 | 99.82 | 88.90 | 99.37 | 99.78 |
| 8 | 88.66 | 85.41 | 85.36 | 90.00 | 93.92 | 93.91 | 86.73 | 94.23 | 95.85 |
| 9 | 95.15 | 98.00 | 99.33 | 97.94 | 98.86 | 100.00 | 89.35 | 100.00 | 100.00 |
| 10 | 90.66 | 97.99 | 98.08 | 97.18 | 95.74 | 91.84 | 86.16 | 93.49 | 94.69 |
| 11 | 88.58 | 92.70 | 94.55 | 93.08 | 95.38 | 97.01 | 84.85 | 91.58 | 99.51 |
| 12 | 92.07 | 96.97 | 99.52 | 98.57 | 99.85 | 99.89 | 81.05 | 98.18 | 99.96 |
| 13 | 76.07 | 92.68 | 99.23 | 89.40 | 98.94 | 93.06 | 70.16 | 87.20 | 98.17 |
| 14 | 87.35 | 93.23 | 92.40 | 95.68 | 95.39 | 98.64 | 78.05 | 97.37 | 98.10 |
| 15 | 83.55 | 76.41 | 82.45 | 83.89 | 81.80 | 91.56 | 75.92 | 89.47 | 92.83 |
| 16 | 92.54 | 99.50 | 99.90 | 99.83 | 99.85 | 96.12 | 89.57 | 99.32 | 98.13 |

of small target objects for classification. Specifically, for all datasets, the classification results of the AMGCFN method are only lower than those of the proposed MRSGFN method. This is because the cascaded structure of AMGCFN's multihop graph and multiscale convolution can extract richer spatial information, and fully fuse the features of the two subnetworks for classification through attention cross fusion. However, the receptive field of GCN is relatively small, and AMGCFN is prone to misclassification of edge pixels of adjacent features. For example, on the Indian Pines dataset, AMGCFN misclassifies "Grass Press" as "Soybean mintill." On the Pavia dataset, compared with the proposed MRSGFN method, the category visualization results of AMGCFN are closer to that of the real land map, for example: "Meadows" and "Bitumen." In

the Salinas dataset, the proposed MRSGFN method achieved a 100% classification result for the "Fallow Smooth" and "Fallow" categories, which are consistent with the distribution of "Fallow Smooth" and "Fallow" in real land classification maps.

To further validate the classification performance of the proposed MRSGFN method, the t-distributed stochastic neighbor embedding (t-SNE) visualization method were conducted on the Indian Pines, Pavia, and Salinas datasets with the comparison methods FECNet, CTMixer, CEGCN, FDGC, AMGCFN, and the proposed MRSGFN method. From Figs. 12–14, it can be seen that the clustering effect of the proposed MRSGFN method is the most outstanding. Compared to the CNN-based method FECNet and the transformer-based method CTMixer,

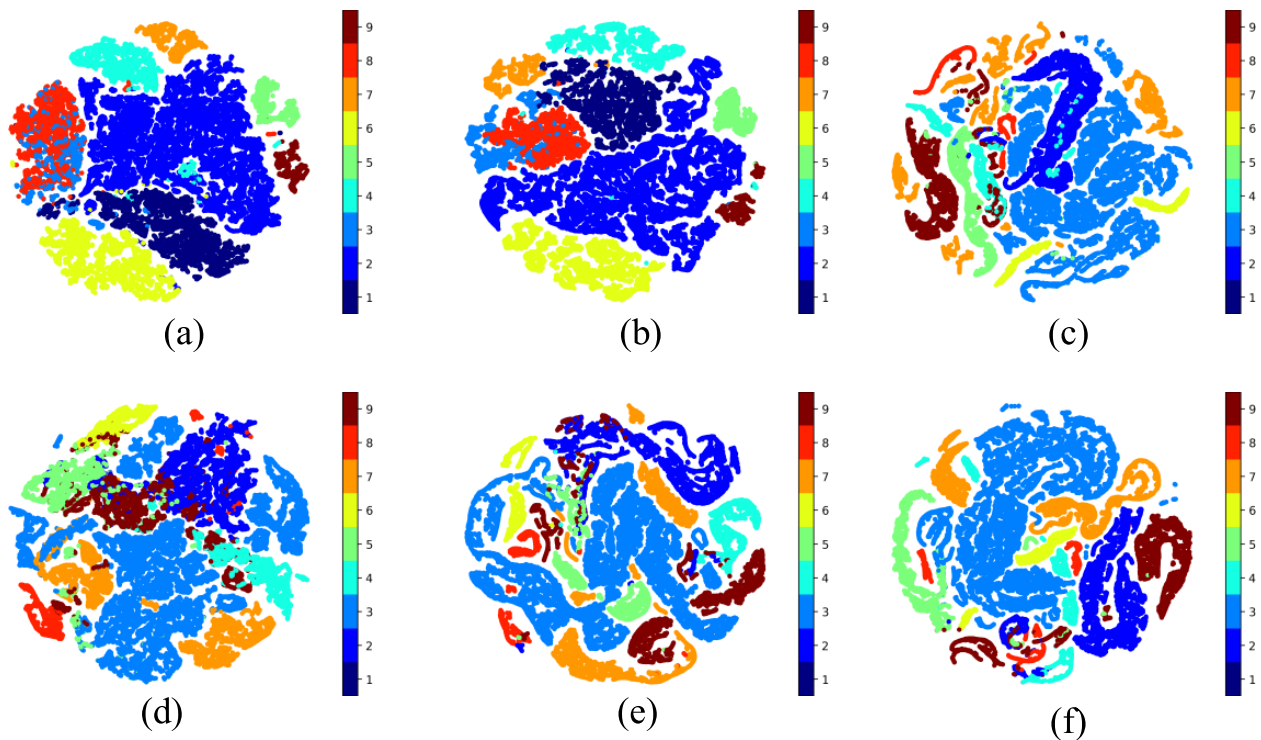


Fig. 13. Comparison of t-SNE visualization results on the Pavia dataset. (a)–(f) Visualization results of t-SNE for FECNet, CTMixer, CEGCN, FDGC, AMGCFN, and MRSGFN, respectively.

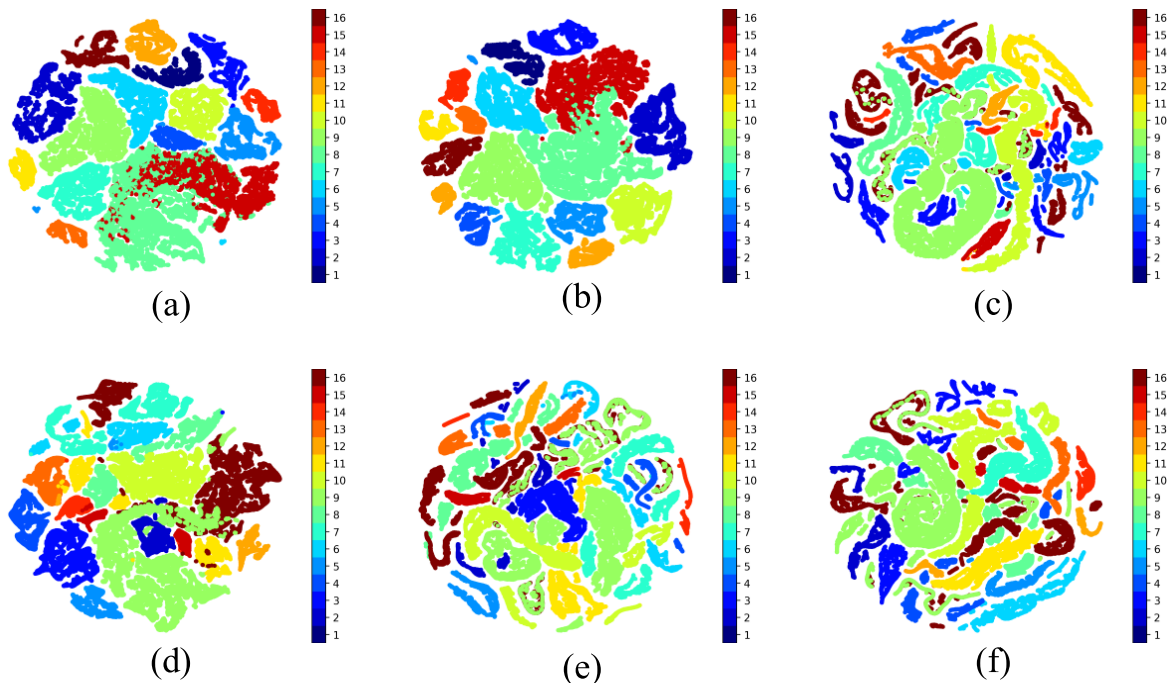


Fig. 14. Comparison of t-SNE visualization results on the Salinas dataset. (a)–(f) Visualization results of t-SNE for FECNet, CTMixer, CEGCN, FDGC, AMGCFN, and MRSGFN, respectively.

the proposed MRSGFN method has a smaller intraclass distance and better clustering performance on the Indian Pine dataset. For the Pavia and Salinas datasets, compared with the GCN-based methods, the proposed MRSGFN method has less category confusion and larger interclass distance, which can better classify different land cover categories. For the Salinas dataset, compared with other methods, the MRSGFN method proposed in this article has the best clustering performance,

with small intraclass distances and larger distances between different categories.

IV. CONCLUSION

In this article, in order to solve the classification problem of HSIs under small samples, a MRSGFN for HSI classification is proposed. MRSGFN consists of three core modules, that is, MHRA, SI2FEM based on spectral overlap grouping, and

GWFM. In the graph integration branch, the receptive field of GCN is expanded by MHRA through high-order hop graph in an attention-weighted manner. In order to solve the problem of dimensionality disaster more prominent due to the high spectral dimensions in small samples, a SI2FEM is proposed. SI2FEM reduces spectral dimensionality through spectral grouping while preserving important spectral information, and extracts intra- and intergroup spectral features from the grouped data. Finally, in order to better integrate the features extracted from the two branches, a GWFM is proposed. GWFM assigns different weights to the features extracted from the convolutional branch and graph convolutional branch through 2-D Gaussian mapping, and then fuses these features based on the assigned weights. Experiments on three common datasets show that the MRSGFN proposed in this article has excellent feature extraction and fusion abilities compared to other advanced classification methods.

In future work, we will focus on graph convolution and transformer, combining the advantages of graph convolution in extracting local features with the global receptive field of transformer, further enhancing the feature learning ability of the designed network, and improving the classification performance of HSI. Moreover, we will do some research on the models of graph-transformer in semisupervised scenarios, aiming to solve the problem of hyperspectral image classifications (HSIC) with fewer labeled samples and higher sample labeling costs.

REFERENCES

- [1] S. S. M. Noor, K. Michael, S. Marshall, J. Ren, J. Tschannerl, and F. J. Kao, "The properties of the cornea based on hyperspectral imaging: Optical biomedical engineering perspective," in *Proc. Int. Conf. Syst., Signals Image Process. (IWSSIP)*, May 2016, pp. 1–4.
- [2] U. Khan, S. Paheding, C. P. Elkin, and V. K. Devabhaktuni, "Trends in deep learning for medical hyperspectral image analysis," *IEEE Access*, vol. 9, pp. 79534–79548, 2021.
- [3] C. M. Gevaert, J. Suomalainen, J. Tang, and L. Kooistra, "Generation of spectral-temporal response surfaces by combining multispectral satellite and hyperspectral UAV imagery for precision agriculture applications," *IEEE J. Sel. Topics Appl. Earth Observ. Remote Sens.*, vol. 8, no. 6, pp. 3140–3146, Jun. 2015.
- [4] Z. Chao, F. Xianchuang, W. Tong, Z. Yuanzhi, and C. Shengbo, "Detection of ore-forming elements migrated from rock and soil to vegetation leaves using hyperspectral data," *Radio Sci.*, vol. 58, no. 8, pp. 1–9, Aug. 2023.
- [5] X. Zheng, Y. Yuan, and X. Lu, "A deep scene representation for aerial scene classification," *IEEE Trans. Geosci. Remote Sens.*, vol. 57, no. 7, pp. 4799–4809, Jul. 2019.
- [6] X. Zheng, B. Wang, X. Du, and X. Lu, "Mutual attention inception network for remote sensing visual question answering," *IEEE Trans. Geosci. Remote Sens.*, vol. 60, pp. 1–14, 2022, Art. no. 5606514.
- [7] Y. Duan, F. Luo, M. Fu, Y. Niu, and X. Gong, "Classification via structure-preserved hypergraph convolution network for hyperspectral image," *IEEE Trans. Geosci. Remote Sens.*, vol. 61, pp. 1–13, 2023, Art. no. 5507113.
- [8] X. Zheng, T. Gong, X. Li, and X. Lu, "Generalized scene classification from small-scale datasets with multitask learning," *IEEE Trans. Geosci. Remote Sens.*, vol. 60, pp. 1–11, 2022, Art. no. 5609311.
- [9] X. Zheng, X. Chen, X. Lu, and B. Sun, "Unsupervised change detection by cross-resolution difference learning," *IEEE Trans. Geosci. Remote Sens.*, vol. 60, pp. 1–16, 2022, Art. no. 5606616.
- [10] X. Zheng, H. Sun, X. Lu, and W. Xie, "Rotation-invariant attention network for hyperspectral image classification," *IEEE Trans. Image Process.*, vol. 31, pp. 4251–4265, 2022.
- [11] Y. Duan, H. Huang, and T. Wang, "Semisupervised feature extraction of hyperspectral image using nonlinear geodesic sparse hypergraphs," *IEEE Trans. Geosci. Remote Sens.*, vol. 60, pp. 1–15, 2022, Art. no. 5515115.
- [12] Y. Dong, Q. Liu, B. Du, and L. Zhang, "Weighted feature fusion of convolutional neural network and graph attention network for hyperspectral image classification," *IEEE Trans. Image Process.*, vol. 31, pp. 1559–1572, 2022.
- [13] J. Bai, B. Ding, Z. Xiao, L. Jiao, H. Chen, and A. C. Regan, "Hyperspectral image classification based on deep attention graph convolutional network," *IEEE Trans. Geosci. Remote Sens.*, vol. 60, 2022, Art. no. 5504316.
- [14] L. Fang, D. Zhu, J. Yue, B. Zhang, and M. He, "Geometric-spectral reconstruction learning for multi-source open-set classification with hyperspectral and LiDAR data," *IEEE/CAA J. Autom. Sinica*, vol. 9, no. 10, pp. 1892–1895, Oct. 2022.
- [15] R. Hang, X. Qian, and Q. Liu, "Cross-modality contrastive learning for hyperspectral image classification," *IEEE Trans. Geosci. Remote Sens.*, vol. 60, pp. 1–12, 2022, Art. no. 5532812.
- [16] L. Mou, P. Ghamisi, and X. X. Zhu, "Deep recurrent neural networks for hyperspectral image classification," *IEEE Trans. Geosci. Remote Sens.*, vol. 55, no. 7, pp. 3639–3655, Jul. 2017.
- [17] Y. Chen, H. Jiang, C. Li, X. Jia, and P. Ghamisi, "Deep feature extraction and classification of hyperspectral images based on convolutional neural networks," *IEEE Trans. Geosci. Remote Sens.*, vol. 54, no. 10, pp. 6232–6251, Oct. 2016.
- [18] A. Santara et al., "BASS Net: Band-adaptive spectral-spatial feature learning neural network for hyperspectral image classification," *IEEE Trans. Geosci. Remote Sens.*, vol. 55, no. 9, pp. 5293–5301, Sep. 2017.
- [19] W. Song, S. Li, L. Fang, and T. Lu, "Hyperspectral image classification with deep feature fusion network," *IEEE Trans. Geosci. Remote Sens.*, vol. 56, no. 6, pp. 3173–3184, Jun. 2018.
- [20] H. Lee and H. Kwon, "Going deeper with contextual CNN for hyperspectral image classification," *IEEE Trans. Image Process.*, vol. 26, no. 10, pp. 4843–4855, Oct. 2017.
- [21] M. E. Paoletti, J. M. Haut, R. Fernandez-Beltran, J. Plaza, A. J. Plaza, and F. Pla, "Deep pyramidal residual networks for spectral-spatial hyperspectral image classification," *IEEE Trans. Geosci. Remote Sens.*, vol. 57, no. 2, pp. 740–754, Feb. 2019.
- [22] S. K. Roy, S. Manna, T. Song, and L. Bruzzone, "Attention-based adaptive spectral-spatial kernel ResNet for hyperspectral image classification," *IEEE Trans. Geosci. Remote Sens.*, vol. 59, no. 9, pp. 7831–7843, Sep. 2021.
- [23] Y.-L. Wei, Y.-B. Zheng, R. Wang, and H.-C. Li, "Quaternion convolutional neural network with EMAP representation for multisource remote-sensing data classification," *IEEE Geosci. Remote Sens. Lett.*, vol. 20, pp. 1–5, 2023.
- [24] C. Shi, D. Liao, T. Zhang, and L. Wang, "Hyperspectral image classification based on expansion convolution network," *IEEE Trans. Geosci. Remote Sens.*, vol. 60, pp. 1–16, 2022, Art. no. 5528316.
- [25] J. Zhu, L. Fang, and P. Ghamisi, "Deformable convolutional neural networks for hyperspectral image classification," *IEEE Geosci. Remote Sens. Lett.*, vol. 15, no. 8, pp. 1254–1258, Aug. 2018.
- [26] J. He, L. Zhao, H. Yang, M. Zhang, and W. Li, "HSI-BERT: Hyperspectral image classification using the bidirectional encoder representation from transformers," *IEEE Trans. Geosci. Remote Sens.*, vol. 58, no. 1, pp. 165–178, Jan. 2020.
- [27] X. Yang, W. Cao, Y. Lu, and Y. Zhou, "Hyperspectral image transformer classification networks," *IEEE Trans. Geosci. Remote Sens.*, vol. 60, 2022, Art. no. 5528715.
- [28] L. Sun, G. Zhao, Y. Zheng, and Z. Wu, "Spectral-spatial feature tokenization transformer for hyperspectral image classification," *IEEE Trans. Geosci. Remote Sens.*, vol. 60, 2022, Art. no. 5522214.
- [29] D. Hong et al., "SpectralFormer: Rethinking hyperspectral image classification with transformers," *IEEE Trans. Geosci. Remote Sens.*, vol. 60, 2022, Art. no. 5518615.
- [30] S. Wan, C. Gong, P. Zhong, B. Du, L. Zhang, and J. Yang, "Multiscale dynamic graph convolutional network for hyperspectral image classification," *IEEE Trans. Geosci. Remote Sens.*, vol. 58, no. 5, pp. 3162–3177, May 2020.
- [31] W. Yu, S. Wan, G. Li, J. Yang, and C. Gong, "Hyperspectral image classification with contrastive graph convolutional network," *IEEE Trans. Geosci. Remote Sens.*, vol. 61, pp. 1–15, 2023, Art. no. 5503015.
- [32] S. Wan, C. Gong, P. Zhong, S. Pan, G. Li, and J. Yang, "Hyperspectral image classification with context-aware dynamic graph convolutional network," *IEEE Trans. Geosci. Remote Sens.*, vol. 59, no. 1, pp. 597–612, Jan. 2021.

- [33] Z. Zhao, H. Wang, and X. Yu, "Spectral-spatial graph attention network for semisupervised hyperspectral image classification," *IEEE Geosci. Remote Sens. Lett.*, vol. 19, pp. 1–5, 2022.
- [34] Y. Ding, X. Zhao, Z. Zhang, W. Cai, and N. Yang, "Graph sample and aggregate-attention network for hyperspectral image classification," *IEEE Geosci. Remote Sens. Lett.*, vol. 19, pp. 1–5, 2022.
- [35] F. F. Shahraiki and S. Prasad, "Graph convolutional neural networks for hyperspectral data classification," in *Proc. IEEE Global Conf. Signal Inf. Process. (GlobalSIP)*, Shahrak, CA, USA, Nov. 2018, pp. 968–972.
- [36] A. Qin, C. Liu, Z. Shang, and J. Tian, "Spectral-spatial graph convolutional networks for semel-supervised hyperspectral image classification," in *Proc. Int. Conf. Wavelet Anal. Pattern Recognit. (ICWAPR)*, Chengdu, China, Jul. 2018, pp. 89–94.
- [37] Q. Liu, Y. Dong, Y. Zhang, and H. Luo, "A fast dynamic graph convolutional network and CNN parallel network for hyperspectral image classification," *IEEE Trans. Geosci. Remote Sens.*, vol. 60, 2022, Art. no. 5530215.
- [38] H. Zhou, F. Luo, H. Zhuang, Z. Weng, X. Gong, and Z. Lin, "Attention multihop graph and multiscale convolutional fusion network for hyperspectral image classification," *IEEE Trans. Geosci. Remote Sens.*, vol. 61, 2023, Art. no. 5508614.
- [39] P.-T. Jiang, Q. Hou, Y. Cao, M.-M. Cheng, Y. Wei, and H. Xiong, "Integral object mining via online attention accumulation," in *Proc. IEEE/CVF Int. Conf. Comput. Vis. (ICCV)*, Oct. 2019, pp. 2070–2079.
- [40] Q. Liu, L. Xiao, J. Yang, and Z. Wei, "CNN-enhanced graph convolutional network with pixel- and superpixel-level feature fusion for hyperspectral image classification," *IEEE Trans. Geosci. Remote Sens.*, vol. 59, no. 10, pp. 8657–8671, Oct. 2021.
- [41] S. K. Roy, G. Krishna, S. R. Dubey, and B. B. Chaudhuri, "HybridSN: Exploring 3-D–2-D CNN feature hierarchy for hyperspectral image classification," *IEEE Geosci. Remote Sens. Lett.*, vol. 17, no. 2, pp. 277–281, Feb. 2020.
- [42] J. Zhang, Z. Meng, F. Zhao, H. Liu, and Z. Chang, "Convolution transformer mixer for hyperspectral image classification," *IEEE Geosci. Remote Sens. Lett.*, vol. 19, pp. 1–5, 2022.
- [43] X. Tang, T. Zhang, J. Ma, X. Zhang, F. Liu, and L. Jiao, "WNet: W-Shaped hierarchical network for remote-sensing image change detection," *IEEE Trans. Geosci. Remote Sens.*, vol. 61, pp. 1–14, 2023, Art. no. 5615814.
- [44] R. Ji, K. Tan, X. Wang, C. Pan, and L. Xin, "PASSNet: A spatial-spectral feature extraction network with patch attention module for hyperspectral image classification," *IEEE Geosci. Remote Sens. Lett.*, vol. 20, pp. 1–5, 2023, Art. no. 5510405.
- [45] X. Wang, K. Tan, P. Du, C. Pan, and J. Ding, "A unified multiscale learning framework for hyperspectral image classification," *IEEE Trans. Geosci. Remote Sens.*, vol. 60, 2022.
- [46] M. Zhu, J. Fan, Q. Yang and T. Chen, "SC-EADNet: A Self-supervised contrastive efficient asymmetric dilated network for hyperspectral image classification," *IEEE Trans. Geosci. Remote Sens.*, vol. 60, pp. 1–17, 2022, Art. no. 5519517.
- [47] Q. Liu et al., "Refined prototypical contrastive learning for few-shot hyperspectral image classification," *IEEE Trans. Geosci. Remote Sens.*, vol. 61, 2023, Art. no. 5506214.
- [48] Z. Xu, W. Jiang, and J. Geng, "Dual-branch dynamic modulation network for hyperspectral and LiDAR data classification," *IEEE Trans. Geosci. Remote Sens.*, vol. 61, pp. 1–13, 2023, Art. no. 5514813.



Shuheng Yue received the bachelor's degree from Shandong Jiaotong University, Jinan, China, in 2021. He is currently pursuing the master's degree with Qiqihar University, Qiqihar, China.

His research interests include hyperspectral image processing and machine learning.



Haiyang Wu received the bachelor's degree from Jinjiang College, Sichuan University, Chengdu, Sichuan, China, in 2021. He is currently pursuing the master's degree with Qiqihar University, Qiqihar, China.

His research interests include hyperspectral image processing and machine learning.



Fei Zhu received the bachelor's degree from Luoyang Institute of Science and Technology, Luoyang, China, in 2021. He is currently pursuing the master's degree with Qiqihar University, Qiqihar, China.

His research interests include hyperspectral image processing and machine learning.



Cuiping Shi (Member, IEEE) received the M.S. degree from Yangzhou University, Yangzhou, China, in 2007, and the Ph.D. degree from Harbin Institute of Technology, Harbin, China, in 2016.

From 2017 to 2020, she was a Post-Doctoral Researcher with Harbin Engineering University, Harbin. She is currently a Professor and works with the College of Information Engineering, Huzhou University, Huzhou, China. She has published two academic books and more than 80 papers in journals and conference proceedings. Her main research

interests include remote sensing image processing.



Ligu Wang (Member, IEEE) received the M.S. and Ph.D. degrees in signal and information processing from Harbin Institute of Technology, Harbin, China, in 2002 and 2005, respectively.

From 2006 to 2008, he was a Post-Doctoral Researcher with Harbin Engineering University, Harbin, China. Since 2020, he has been working with the College of Information and Communication Engineering, Dalian Nationalities University, Dalian, China. He has published two books about hyperspectral image processing and more than 130 papers

in journals and conference proceedings. His main research interests include remote sensing image processing.



本次查收索引工作是根据委托人提供的作者姓名、组织机构及文献列表进行的, 委托人信息如下:

姓名: 石翠萍

机构: 齐齐哈尔大学

检索范围:

- 科学引文索引 (Science Citation Index Expanded): 1900年-2024年
- 期刊引证报告 (Journal Citation Reports): 1997年-2023年
- 中科院期刊分区表: 2005年-2023年

检索结果:

| 检索类型 | 数据库 | 年份范围 | 记录数 |
|----------|--------------|-------------|-----|
| SCI-E 收录 | SCI-EXPANDED | 2024 | 1 |
| JCR 影响因子 | JCR | 1997 - 2023 | 1 |
| 中科院期刊分区 | 中科院分区 | 2005 - 2023 | 1 |



2024年9月9日

附件一: SCI-E 收录

| # | 作者 | 标题 | 来源出版物 | JCR影响因子 | 中科院分区 | 文献类型 | 入藏号 |
|----|--|--|---|---------------|--|-----------|---------------------|
| 1 | Shi, CP; Yue, SH; Wu, HY; Zhu, F; Wang, LG | A Multihop Graph Rectify Attention and Spectral Overlap Grouping Convolutional Fusion Network for Hyperspectral Image Classification | IEEE TRANSACTIONS ON GEOSCIENCE AND REMOTE SENSING 2024, 62: 5520517. | • 7.5 (2023); | • 小类(升级版) (2023) 遥感 [2区]; • 小类(升级版) (2023) 成像科学与照相技术 [2区]; • 小类(升级版) (2023) 工程: 电子与电气 [2区]; • 小类(升级版) (2023) 地球化学与地球物理 [1区]; • 大类(升级版) (2023) 地球科学 [1区]; | J Article | WOS:001294607700025 |
| 合计 | | | | | | | 1 |

第 1 条, 共 1 条:

标题: A Multihop Graph Rectify Attention and Spectral Overlap Grouping Convolutional Fusion Network for Hyperspectral Image Classification

作者: Shi, CP (Shi, Cuiping); Yue, SH (Yue, Shuheng); Wu, HY (Wu, Haiyang); Zhu, F (Zhu, Fei); Wang, LG (Wang, Ligu)

来源出版物: IEEE TRANSACTIONS ON GEOSCIENCE AND REMOTE SENSING 卷: 62 文献号: 5520517 出版年: 2024

入藏号: WOS:001294607700025

文献类型: Article 出版物类型: J

作者地址: [Shi, Cuiping; Yue, Shuheng; Wu, Haiyang; Zhu, Fei] Qiqihar Univ, Dept Commun Engn, Qiqihar 161000, Peoples R China.; [Shi, Cuiping] Huzhou Univ, Coll Informat Engn, Huzhou 313000, Peoples R China.; [Wang, Ligu] Dalian Nationalities Univ, Coll Informat & Commun Engn, Dalian 116000, Peoples R China.

所属机构: Qiqihar University; Huzhou University; Dalian Minzu University

通讯作者地址: Shi, CP (corresponding author), Qiqihar Univ, Dept Commun Engn, Qiqihar 161000, Peoples R China.; Shi, CP (corresponding author), Huzhou Univ, Coll Informat Engn, Huzhou 313000, Peoples R China.

电子邮件地址: shicuiping@qqhru.edu.cn; 2021910320@qqhru.edu.cn; 2021910323@qqhru.edu.cn; 2022935750@qqhru.edu.cn; wangliguo@hrbeu.edu.cn

出版商: IEEE-INST ELECTRICAL ELECTRONICS ENGINEERS INC 出版商城市: PISCATAWAY 出版商地址: 445 HOES LANE, PISCATAWAY, NJ 08855-4141 USA

Web of Science 类别: Geochemistry & Geophysics; Engineering, Electrical & Electronic; Remote Sensing; Imaging Science & Photographic Technology
研究方向: Geochemistry & Geophysics; Engineering; Remote Sensing; Imaging Science & Photographic Technology

IDS 号: D2N5T

ISSN: 0196-2892 eISSN: 1558-0644

基金资助机构和授权号: National Natural Science Foundation of China

基金资助致谢: No Statement Available

JCR 影响因子:

| 期刊 | JCR 影响因子 | 指标年份 |
|--|----------|------|
| IEEE TRANSACTIONS ON GEOSCIENCE AND REMOTE SENSING | 7.5 | 2023 |

中科院期刊分区:

| 期刊 | 类型 | 学科类别 | 分区 | 指标年份 | TOP |
|--|---------|--|----|------|-----|
| IEEE TRANSACTIONS ON GEOSCIENCE AND REMOTE SENSING | 大类(升级版) | 地球科学 | 1 | 2023 | 否 |
| IEEE TRANSACTIONS ON GEOSCIENCE AND REMOTE SENSING | 小类(升级版) | 工程: 电子与电气 (ENGINEERING, ELECTRICAL & ELECTRONIC) | 2 | 2023 | - |
| IEEE TRANSACTIONS ON GEOSCIENCE AND REMOTE SENSING | 小类(升级版) | 地球化学与地球物理 (GEOCHEMISTRY & GEOPHYSICS) | 1 | 2023 | - |
| IEEE TRANSACTIONS ON GEOSCIENCE AND REMOTE SENSING | 小类(升级版) | 成像科学与照相技术 (IMAGING SCIENCE & PHOTOGRAPHIC TECHNOLOGY) | 2 | 2023 | - |
| IEEE TRANSACTIONS ON GEOSCIENCE AND REMOTE SENSING | 小类(升级版) | 遥感 (REMOTE SENSING) | 2 | 2023 | - |

End